

A Bayesian Mark Interaction Model for Analysis of Tumor Pathology Images

Qiwei Li

Department of Clinical Sciences

University of Texas Southwestern Medical Center, Dallas, Texas

and

Xinlei Wang

Department of Statistics

Southern Methodist University, Dallas Texas

and

Faming Liang

Department of Statistics

Purdue University, West Lafayette, Indiana

and

Guanghua Xiao*

Department of Clinical Sciences

University of Texas Southwestern Medical Center, Dallas, Texas

November 22, 2021

*To whom correspondence should be addressed.

Abstract

With the advance of imaging technology, digital pathology imaging of tumor tissue slides is becoming a routine clinical procedure for cancer diagnosis. This process produces massive imaging data that capture histological details in high resolution. Recent developments in deep-learning methods have enabled us to identify and classify individual cells from digital pathology images at large scale. The randomly distributed cells can be considered from a marked point process, where each point is defined by its position and cell type. Reliable statistical approaches to model such marked spatial point patterns can provide new insight into tumor progression and shed light on the biological mechanisms of cancer. In this paper, we consider the problem of modeling spatial correlations among three commonly seen cells (i.e. lymphocyte, stromal, and tumor) observed in tumor pathology images. A novel marking model of marked point processes, with interpretable underlying parameters (some of which are clinically meaningful), is proposed in a Bayesian framework. We use Markov chain Monte Carlo (MCMC) sampling techniques, combined with the double Metropolis-Hastings (DMH) algorithm, to sample from the posterior distribution with an intractable normalizing constant. On the benchmark datasets, we demonstrate how this model-based analysis can lead to sharper inferences than ordinary exploratory analyses. Lastly, we conduct a case study on the pathology images of 188 lung cancer patients from the National Lung Screening Trial. The results show that the spatial correlation between tumor and stromal cells predicts patient prognosis. This statistical methodology not only presents a new model for characterizing spatial correlations in a multi-type spatial point pattern, but also provides a new perspective for understanding the role of cell-cell interactions in cancer progression.

Keywords: Marked point process, spatial point pattern, spatial correlation, Markov random field, double Metropolis-Hastings

1 Introduction

Cancer is a complex disease characterized by uncontrolled tumor cell growth. Pathological examination of H&E-stained tissue slides is an essential step in cancer diagnosis. It has been reported that cell growth patterns are associated with the survival outcome (Gleason et al., 2002; Amin et al., 2002; Borczuk et al., 2009; Barletta et al., 2010) and treatment response (Tsao et al., 2015) of cancer patients. In addition, the interactions between tumor cells and other types of cells (e.g. immune cells) play vital roles in the progression and metastasis of cancer (Mantovani et al., 2002; Orimo et al., 2005; Merlo et al., 2006; Polyak et al., 2009; Hanahan and Weinberg, 2011; Gillies et al., 2012; Junttila and de Sauvage, 2013). Spatial variations among cell types and their association with patient prognosis have been previously reported in breast cancer (Mattfeldt et al., 2009). Pathological examination of tissue slides requires a pathologist to match the observed image slides with his/her memory for certain patterns and features (such as tumor content, nuclei counts and tumor boundary). This process is laborious, tedious and subject to errors. More importantly, due to the limitations of the human brain in interpreting highly-complex pathology images, it is extremely hard for pathologists to systematically explore those subtle but essential patterns, such as tumor cell distribution and interaction with the surrounding micro-environment. Pathological examination by the human eyes is insufficient to decipher the large amount of complex and comprehensive information harbored in the high resolution pathology images.

With the advance of imaging technology, H&E-stained pathology imaging is becoming a routine clinical procedure, which produces massive digital pathology images on a daily basis. Recent studies (Beck et al., 2011; Yuan et al., 2012; Luo et al., 2016; Yu et al., 2016) have demonstrated the feasibility of using digital pathology image analysis to assist pathologists in clinical diagnosis and prognosis. However, current studies of pathology image analysis

mainly focus on the morphology features, such as tissue texture and granularity. These imaging data, which capture histological details in high resolution, still leave unexplored more undiscovered knowledge. Computer vision and machine learning algorithms have enabled us to automatically identify and classify individual cells from digital pathology images at large scale (e.g. Yuan et al., 2012). Recent developments in deep-learning methods have greatly facilitated this process. We have developed a convolutional neural network (CNN) to identify individual cells and classify the cell types into three categories: lymphocyte (a type of immune cell), stromal, and tumor.

Consequently, a pathology image is abstracted into a spatial map of marked points, where each cell (i.e. points in the spatial map) belongs to one of the three distinct types (i.e. qualitative marks), and the spatial location of each cell is known. The analysis of pathology images thus becomes an investigation of those spatial maps, which will provide a new perspective for the role of cell-cell interactions in cancer progression. Currently, a patient cohort usually contains hundreds of patients, and each patient has one or more pathology images. These rich datasets provide a great opportunity to study the cell-cell interactions in cancer. Recently, Li et al. (2017) developed a modified Potts model to study the spatial patterns observed in tumor pathology images, by projecting irregularly distributed cells into a 2-dimensional lattice. However, this approximate method relies on selection of an *ad hoc* lattice. More importantly, this method models the interaction among different regions (small squares defined by the lattice), but not those among individual cells.

The study of interactions between objects, which results in the spatial correlation of marks, has been a primary focus in spatial statistics. It is a key aspect in population forestry (Stoyan and Penttinen, 2000) and ecology (Dale, 2000) theory, but receives little attention in biology. Illian et al. (2008) discussed in detail a large variety of numerical, functional, and second-order summary characteristics, which can be used to describe the spatial depen-

dency between different types of points in a planar region. The most common approaches are based on generalizing the standard distance-dependent G-, K-, J-, and L-functions to their “cross-type” versions (see e.g. Ripley, 1977; Besag, 1977; Diggle and Cox, 1981; Lotwick and Silverman, 1982; Diggle and Milne, 1983; Vincent and Jeulin, 1989; Lieshout and Baddeley, 1996; Van Lieshout and Baddeley, 1999). Mark connection functions (MCFs) are another well recognized tool for qualitative marks, which are more suitable for the detection of mark correlation in an exploratory analysis (Wiegand and A Moloney, 2004). The *ad hoc* testing of hypotheses, such as spatial independences of the marks, based on some suitable summary characteristics (e.g. K-functions) has also been discussed in the literature (Grabarnik et al., 2011). However, model-based analysis, which may sharpen inferences about the spatial pattern, is lagging. Diggle et al. (2006) formulated a pairwise interaction model for a spatial pattern of bivariate marked points and argued that model-based inference is statistically more efficient.

In this paper, motivated by the emerging needs of tumor pathology images analysis, we develop a novel marking model, which aims to study the mark formulation in a spatial pattern through a Bayesian framework. A local energy function of three groups of parameters, i.e. first- and second-order intensities, and an exponential decay rate to the inter-point distance, is carefully defined, as is the related Gibbs distribution. The proposed model can serve as a novel model-based approach to characterize the spatial pattern/correlation among marks. We use the double Metropolis-Hastings (DMH) algorithm (Liang, 2010) to sample from the posterior distribution with an intractable normalizing constant in the Gibbs distribution. The model performs well in simulated studies and three benchmark datasets. We also conduct a case study on a large cohort of lung cancer pathology images. The result shows that the spatial correlation between tumor and stromal cells is significantly associated with patient prognosis (P -value=0.0021). Although the morphological features

of stroma in tumor regions have been discovered to be associated with patient survival, there is no strong statistical evidence to support this, due to a lack of rigorous statistical methodology. In the study, the proposed statistical methodology not only delivers a new perspective for understanding how marks (i.e. cell types in pathology images) formulate in marked point processes, but also provides a refined statistical tool to characterize spatial interactions, which the existing approaches (e.g. MCF) may lack sufficient power to do so.

The remainder of the paper is organized as follows: Section 2 introduces the proposed modeling framework, including the local energy function and its related Gibbs distribution (i.e. the model likelihood), the choices of priors, and the model interpretation. Section 3 describes the Markov chain Monte Carlo (MCMC) algorithm and discusses the resulting posterior inference. Section 4 assesses performance of the proposed model on simulated data. Section 5 investigates the results of the data analyses from three benchmark datasets and a large cohort of lung cancer pathology images from the National Lung Screening Trial (NLST). Section 6 concludes the paper with some remarks on future research directions.

2 Model

We describe a spatial map of cells in a Cartesian coordinate system, with n observed cells indexed by i . We use $(x_i, y_i) \in \mathbb{R}^2$ to denote the x - and y - coordinates and $z_i \in \{1, \dots, Q\}$, $Q \geq 2$ to denote the type of cell i . In spatial point pattern analysis, such data are considered as multi-type point pattern data, where $(x_1, y_1), \dots, (x_n, y_n)$ are the point locations in a compact subset of the 2-dimensional Euclidean space \mathbb{R}^2 (note that the proposed model can be easily extend to the general case of \mathbb{R}^k , $k \geq 3$) and z_1, \dots, z_n are their associated qualitative (i.e. categorical or discrete) univariate marks. The mark attached to each point indicates which type/class it is (e.g. on/off, case/control, species,

colors, etc.). Without loss of generality, we assume that the data points are restricted within the unit square $[0, 1]^2$. This can be done by rescaling each pair of coordinates (x_i, y_i) to (x'_i, y'_i) , with $x'_i = (x_i - \min\{\mathbf{x}\})/L$ and $y'_i = (y_i - \min\{\mathbf{y}\})/L$. Usually, L is known, defined as the maximum possible Manhattan distance between any two points (both observed and unobserved) in the space. When L is unknown, it can be estimated from the data itself by: 1) roughly setting $L = \max\{\max\{\mathbf{x}\} - \min\{\mathbf{x}\}, \max\{\mathbf{y}\} - \min\{\mathbf{y}\}\}$; or 2) computing the Ripley-Rasson estimator (Ripley and Rasson, 1977) of a rectangle window, given the points, and then setting L equal to the maximum side length of the window.

2.1 Energy Functions

In the analysis of tumor pathology images, cell distribution and cell-cell interaction may reveal important messages about the tumor cell growth and its micro-environment. Therefore, it is of great interest to study the arrangements of cell types associated with the observed cells, given their locations. In spatial point pattern analysis, such a problem is called *marking modeling*, which is to study the formulation of the marks \mathbf{z} in a pattern, given the points (\mathbf{x}, \mathbf{y}) . In this subsection, we explore the formulation of energy functions, accounting for both of the first- and second-order properties of the point data.

At the initial stage, we assume that each point interacts with all other points in the space. A complete undirected graph $G = (V, E)$ can be used to depict their relationships, with V denoting the set of points (i.e. the n observed cells) and E denoting the set of direct interactions (i.e. the $(n - 1)n/2$ cell-cell pairs). We define G as the interaction network and define its potential energy as

$$V(\mathbf{z}|\boldsymbol{\omega}, \boldsymbol{\Theta}) = \sum_q \omega_q \sum_i I(z_i = q) + \sum_q \sum_{q'} \theta_{qq'} \sum_{(i \sim i') \in E} I(z_i = q, z_{i'} = q'), \quad (1)$$

where the notation $(i \sim i')$ denotes that points i and i' are the interacting pair in G (i.e.

they are connected by an edge in G), and I denotes the indicator function. Note that $\theta_{qq'} = \theta_{q'q}$ as the edge between any pairs of points has no orientation. On the right-hand side of Equation (1), the first term can be viewed as the weighted average of the numbers of points with different marks, while the second term can be viewed as the weighted average of the numbers of pairs connecting two points with the same or different marks. In the context of spatial point pattern analysis, the first and second terms are referred to the first- and second-order potentials/characteristics, respectively. Their corresponding parameters

$$\boldsymbol{\omega} = (\omega_1, \dots, \omega_Q) \text{ and } \boldsymbol{\Theta} = \begin{pmatrix} \theta_{11} & \cdots & \theta_{1Q} \\ & \ddots & \vdots \\ & & \theta_{QQ} \end{pmatrix}$$

are defined as the first- and second-order intensities. These two groups of parameters control the enrichment of different marks and the spatial correlations among them simultaneously. A detailed interpretation of $\boldsymbol{\omega}$ and $\boldsymbol{\Theta}$ is discussed in Section 2.4.

In mathematical physics and statistical thermodynamics, the interaction energy between two points (i.e. particles and cells) is usually an exponential decay function with respect to the distance between the two points (see e.g. Penrose and Lebowitz, 1974; Kashima, 2010; Avalos and Bucci, 2014; Chulaevsky, 2014; Rincón et al., 2015). Similarly, exponential decay has also been observed in biological systems, such as cell-cell interactions (Segal and Stephany, 1984; Hui and Bhatia, 2007) and gene-gene correlations (Xiao et al., 2009, 2011). In this study, we assume the interaction energy between a pair of points decreases exponentially at a rate λ proportional to the distance,

$$V(\mathbf{z}|\boldsymbol{\omega}, \boldsymbol{\Theta}, \lambda) = \sum_q \omega_q \sum_i I(z_i = q) + \sum_q \sum_{q'} \theta_{qq'} \sum_{(i \sim i') \in E} e^{-\lambda d_{ii'}} I(z_i = q, z_{i'} = q'), \quad (2)$$

where $d_{ii'} = \sqrt{(x_i - x_{i'})^2 + (y_i - y_{i'})^2}$ is the Euclidean distance between points i and i' . A larger value of the decay parameter λ makes the interaction energy vanish much more

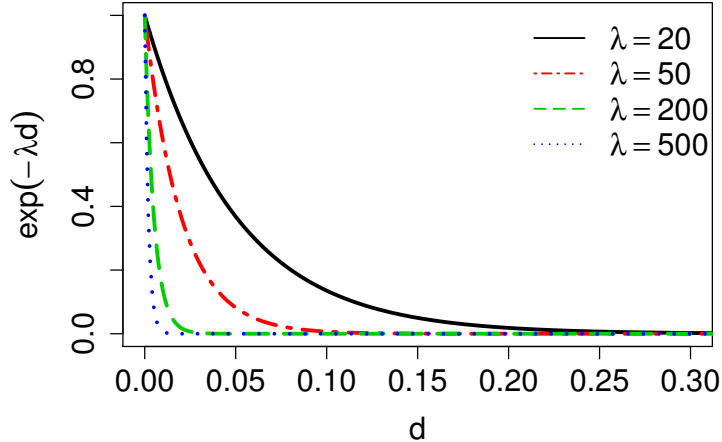


Figure 1: Examples of exponential decay functions under different choices of λ

rapidly with the distance, while a smaller value leads to $e^{-\lambda d_{ii'}} \approx 1$ and Equation (2) \rightarrow Equation (1). See Figure 1 for examples of exponential decay functions with different values of parameter λ .

As shown in Equation (2), it needs to sum over n data points and $(n-1)n/2$ pairs of data points to compute the potential energy, resulting in an extremely tedious computation, especially when n is large. An alternative way is to obtain an approximate value of $V(\mathbf{z}|\boldsymbol{\omega}, \boldsymbol{\Theta}, \lambda)$ by neglecting those pairs with distance beyond a certain threshold c , $c \in [0, 1]$. This is feasible as long as the decay function $e^{-\lambda d}$ causes exponentially decreasing weights for those pairs being placed on the potential energy. It can be illustrated that a point (i.e. a cell) can only interact with its nearby points within a certain range c . Therefore, the complete network G reduces to a sparse network $G' = (V, E')$, with $E' \subseteq E$ denoting the set of edges joining pairs of points i and i' in G' , if their distance $d_{ii'}$ is smaller than a

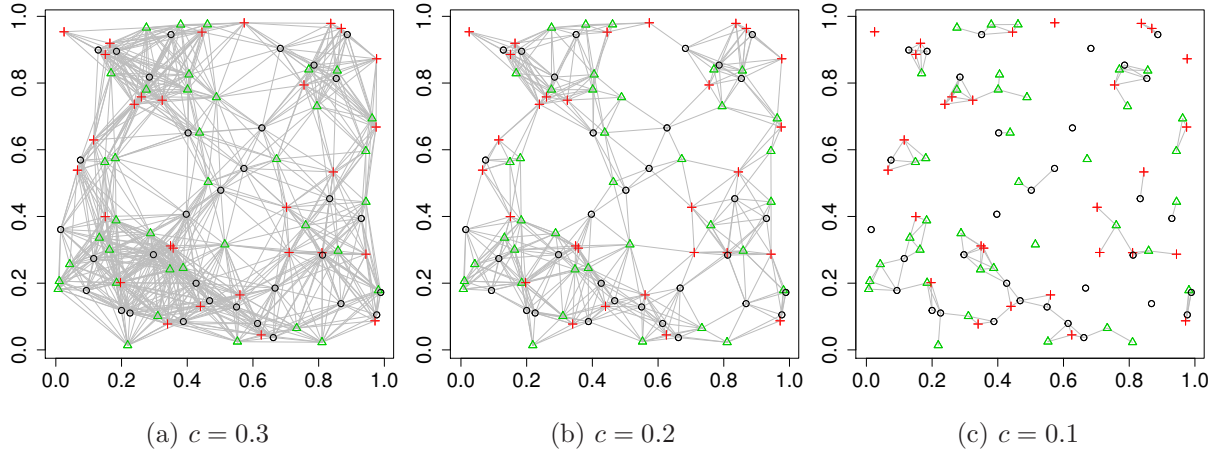


Figure 2: An example of three-type point pattern data ($n = 100$) and its corresponding network G' under different choices of (a) $c = 0.3$, (b) $c = 0.2$, and (c) $c = 0.1$.

threshold c . We write the potential energy of the interaction network G' as

$$V(\mathbf{z}|\boldsymbol{\omega}, \boldsymbol{\Theta}, \lambda) = \sum_q \omega_q \sum_i I(z_i = q) + \sum_q \sum_{q'} \theta_{qq'} \sum_{(i \sim i') \in E'} e^{-\lambda d_{ii'}} I(z_i = q, z_{i'} = q') \quad (3)$$

Note that c is not a model parameter, but a user-defined value. We may determine its value from a mark connection function analysis (discussed in Section 4) or from the subjective assessment of an experienced expert in the related field. The choice of a large c causes an extremely complex network, while a too small value results in a sparse network that may neglect some important spatial information. See Figure 2 for an example of three-type point pattern data ($n = 100$) and its corresponding mark interaction networks G' under different choices of c . By introducing the sparse network G' , we not only reduce the computational cost in calculating the potential energy, but also define a local spatial structure.

2.2 Data Likelihood

According to the fundamental Hammersley-Clifford theorem (Hammersley and Clifford, 1971), if we have a locally defined energy, such as Equation (3), then a probability measure with a Markov property exists. Specifically, this frequently seen measure in many problems of probability theory and statistical mechanics is called a *Gibbs measure*. It gives the probability of observing the marks associated with their locations in a particular state,

$$\begin{aligned}
 p(\mathbf{z}|\boldsymbol{\omega}, \boldsymbol{\Theta}, \lambda) &= \frac{\exp(-V(\mathbf{z}|\boldsymbol{\omega}, \boldsymbol{\Theta}, \lambda))}{\sum_{\mathbf{z}'} \exp(-V(\mathbf{z}'|\boldsymbol{\omega}, \boldsymbol{\Theta}, \lambda))} \\
 &= \frac{1}{C(\boldsymbol{\omega}, \boldsymbol{\Theta}, \lambda)} \exp \left(- \sum_q \omega_q \sum_i I(z_i = q) + \sum_q \sum_{q'} \theta_{qq'} \sum_{(i \sim i') \in E'} e^{-\lambda d_{ii'}} I(z_i = q, z_{i'} = q') \right). \tag{4}
 \end{aligned}$$

The normalizing constant $C(\boldsymbol{\omega}, \boldsymbol{\Theta}, \lambda) = \sum_{\mathbf{z}'} \exp(-V(\mathbf{z}'|\boldsymbol{\omega}, \boldsymbol{\Theta}, \lambda))$ is also called a partition function. An exact evaluation of $C(\boldsymbol{\omega}, \boldsymbol{\Theta}, \lambda)$ needs to sum over the entire space of \mathbf{z} , which consists of Q^n states. Thus, it is intractable even for a small size model. Take $Q = 2$ and $n = 100$ for example, it needs to sum over $2^{100} \approx 1.268 \times 10^{30}$ elements. To address this issue, we employ the double Metropolis-Hastings (DMH) algorithm (Liang, 2010) to make inference on the model parameters $\boldsymbol{\omega}$, $\boldsymbol{\Theta}$, and λ . DMH is an auxiliary variable MCMC algorithm, which can make the normalizing constant ratio canceled by augmenting appropriate auxiliary variables through a short run of the ordinary Metropolis-Hastings (MH) algorithm. More details are given in Section 3.1.

Equation (4) serves as the full data likelihood of the proposed model. Since the model satisfies the local Markov property, we can also write the probability of observing point i belonging to class q conditional on its neighborhood configuration(s),

$$p(z_i = q | \mathbf{z}_{-i}, \boldsymbol{\omega}, \boldsymbol{\Theta}, \lambda) \propto \exp \left(-\omega_q - \sum_{q'} \theta_{qq'} \sum_{\{i': (i \sim i') \in E'\}} e^{-\lambda d_{ii'}} I(z_{i'} = q') \right), \tag{5}$$

where \mathbf{z}_{-i} denotes the the collection of all marks excluding the i -th one. According to Equation (5), the conditional probability depends on the first-order intensity ω_q , the second-order intensities $\theta_{qq'}, q' = 1, \dots, Q$, the decay parameter λ , and the neighborhood of the points defined by c . Although it is not easy to describe how the parameters affect the conditional probability, we can still draw the following conclusions: 1) the smaller the value of ω_q or $\theta_{qq'}$, the more likely that point i belongs to class q ; and 2) the smaller the value of λ , the more impact from the neighborhood configuration(s).

2.3 Parameter Priors

The proposed model in the Bayesian framework requires the specification of prior distributions for the unknown parameters. In this subsection, we specify the priors for all three groups of parameters: $\boldsymbol{\omega}$, $\boldsymbol{\Theta}$, and λ . For the first- and second-order intensities $\boldsymbol{\omega}$ and $\boldsymbol{\Theta}$, we notice that an identifiability problem arises from Equation (4) or (5). For instance, adding a non-zero constant, say s , into $\omega_q, q = 1, \dots, Q$ does not change the probability of observing point i belonging to class q . Similarly, the settings of $\boldsymbol{\Theta}$ and $\boldsymbol{\Theta} + s\mathbf{I}$ lead to the same conditional probability. Therefore, imposing an appropriate constraint is necessary. Without loss of generality, suppose the points with mark Q have the largest population and we set $\omega_Q = 1$ and $\theta_{QQ} = 1$. For the other parameters in $\boldsymbol{\omega}$ and $\boldsymbol{\Theta}$, we consider normal priors and set $\omega_q \sim N(\mu_\omega, \sigma_\omega^2), q = 1, \dots, Q - 1$ and $\theta_{qq'} \sim N(\mu_\theta, \sigma_\theta^2), q = 1, \dots, Q - 1, q' = q, \dots, Q$. We suggest users choose the standard normal distribution; that is, $\mu_\omega = \mu_\theta = 0$ and $\sigma_\omega = \sigma_\theta = 1$. For the decay parameter λ , we specify a gamma prior $\lambda \sim \text{Ga}(a_\lambda, b_\lambda)$. One standard way of setting a weakly informative gamma prior is to choose small values for the two parameters, such as $a_\lambda = b_\lambda = 0.001$ (Gelman et al., 2006).

2.4 Interpretation

In this subsection, we aim to interpret the meanings of the model parameters $\boldsymbol{\omega}$ and $\boldsymbol{\Theta}$, because it is crucial for describing the observed spatial pattern as well as studying their associations with any other measurements of interest.

Suppose there is only one point in the space. Then Equation (5) reduces to $p(z_1 = q|\cdot) \propto \exp(-\omega_q)$, which implies the probability of observing a point with mark q in this single-point system is equal to

$$\pi_q = \exp(-\omega_q) / \sum_q \exp(-\omega_q). \quad (6)$$

Note that the vector $\boldsymbol{\pi} = (\pi_1, \dots, \pi_Q)$ has a natural constraint; that is, $\sum_q \pi_q = 1$. Furthermore, suppose there are n points in the space and there are almost no mark interactions. This can be fulfilled by any one of the following conditions: 1) the distance between any pairs of two points is beyond the given value c , i.e. $d_{ii'} > c, \forall (i \sim i') \in E$; 2) the second-order intensities are all equal, i.e. $\boldsymbol{\Theta} = s\mathbf{1}, \forall s \in \mathbb{R}$; or 3) the decay parameter λ goes to infinity, i.e. $\lambda \rightarrow \infty$. Then Equation (5) converges to $p(z_i = q|\mathbf{z}_{-i}, \boldsymbol{\omega}, \boldsymbol{\Theta}, \lambda) \propto \exp(-\omega_q) = \pi_q$, implying that the expected number of points with mark q is $n\pi_q$. Thus, after transforming the first-order intensities $\boldsymbol{\omega}$ to their probability measures $\boldsymbol{\pi}$, we find a clear path to describe the abundance of different marks in the above simplified situations.

Suppose there are only two points 1 and 2 in the space, with the type of the second point known; say $z_2 = q'$. For convenience, we further assume $\omega_1 = \dots = \omega_Q$. We first consider the case of the two points being at the same location, i.e. $d_{12} = 0$. Then Equation (5) turns out to be $p(z_1 = q|z_2 = q', \cdot) \propto \exp(-\theta_{qq'})$, which implies the probability of observing the point with unknown mark belonging to type q , given the one with the known

mark q' (at the same location), is

$$\phi_{qq'} = \exp(-\theta_{qq'}) / \sum_q \exp(-\theta_{qq'}). \quad (7)$$

We use a Q -by- Q matrix ϕ to denote the collection of $\phi_{qq'}, q = 1, \dots, Q, q' = 1, \dots, Q$. Note that each column in ϕ should be summed to 1 and ϕ is not necessary to be a symmetric matrix as Θ . In this duo-point system (and more complex cases therein), the larger the value of $\phi_{qq'}$, the more likely the points with mark q get attracted to the nearby points with mark q' . Thus, the spatial correlations among marks can be easily interpreted by the probability matrix ϕ .

In the aforementioned duo-point model with known parameters, if the assumption of equivalent first-order intensities is relaxed, then the probability of assigning mark q to point 1 conditional on the mark of point 2 is q' is a strictly monotonic function of their distance d ,

$$\text{MIF}_{q|q'}(d) = \frac{\exp(-\omega_q - \theta_{qq'}e^{-\lambda d})}{\sum_{q''} \exp(-\omega_{q''} - \theta_{q''q'}e^{-\lambda d})}. \quad (8)$$

We call the above equation the *mark interaction function* (MIF) of mark q given mark q' . As the distance increases, its value ultimately converges to π_q . The plot of MIF is a more comprehensive way to describe the spatial correlation/interaction between marks.

In conclusion, π , ϕ , and MIF directly characterize a single point behavior (i.e. the assignment of its mark) in a model with small size, such as $n = 1$ and 2 . However, the observed spatial marked point pattern is a reflection of how each individual point reacts with its neighbors. Note that the mappings from ω to π and from Θ to ϕ are one-to-one/unique, so we can implement this step after obtaining the estimates of ω and Θ .

3 Model Fitting

In this section, we describe the MCMC algorithm for posterior inference. Our inferential strategy allows for simultaneously estimating 1) the first-order intensities $\boldsymbol{\omega}$, which reveal the abundance of different marks; 2) the second-order intensities $\boldsymbol{\Theta}$, which capture the spatial correlation among marks; and 3) the decay parameter λ . We first give the full details of our MCMC algorithm and then discuss the resulting posterior inference.

3.1 MCMC Algorithm

We are interested in estimating $\boldsymbol{\omega}$, $\boldsymbol{\Theta}$, and λ , which define the Gibbs measure based on the local energy function. However, the data likelihood, as shown in Equation (4), includes an intractable normalizing constant $C(\boldsymbol{\omega}, \boldsymbol{\Theta}, \lambda)$, making the Metropolis-Hastings algorithm infeasible in practice. To address this issue, we use the double Metropolis-Hastings algorithm (DMH) proposed by Liang (2010). The DMH is an asymptotic algorithm, which has been shown to produce accurate results by various spatial models. Unlike other auxiliary variable MCMC algorithms (Møller et al., 2006; Murray et al., 2012) that also aim to have the normalizing constant ratio canceled, the DMH sampler is more efficient because: 1) it removes the need for exact sampling; and 2) it does not require drawing the auxiliary variables from a perfect sampler. Liang et al. (2016) also proposed an adaptive exchange algorithm, which generates auxiliary variables via an importance sampling procedure from a Markov chain running in parallel. However, this exact algorithm is more computationally intensive than the DMH.

Update of $\boldsymbol{\omega}$: We update each of $\omega_q, q = 1, \dots, Q - 1$ by using the DMH algorithm. We first propose a new ω_q^* from $N(\omega_q, \tau_\omega^2)$. Next, according to Equation (5), we implement the Gibbs sampler to simulate an auxiliary variable \boldsymbol{z}^* starting from \boldsymbol{z} based on the new

$\boldsymbol{\omega}^*$, where all the elements are the same as $\boldsymbol{\omega}$ excluding the q -th one. The proposed value ω_q^* is then accepted to replace the old value with probability $\min(1, r)$. The Hastings ratio r is given as below,

$$r = \frac{p(\mathbf{z}^*|\boldsymbol{\omega}, \boldsymbol{\Theta}, \lambda)}{p(\mathbf{z}|\boldsymbol{\omega}, \boldsymbol{\Theta}, \lambda)} \frac{p(\mathbf{z}|\boldsymbol{\omega}^*, \boldsymbol{\Theta}, \lambda)}{p(\mathbf{z}^*|\boldsymbol{\omega}^*, \boldsymbol{\Theta}, \lambda)} \frac{N(\omega_q^*; \mu_\omega, \sigma_\omega^2)}{N(\omega_q; \mu_\omega, \sigma_\omega^2)} \frac{J(\omega_q; \omega_q^*)}{J(\omega_q^*; \omega_q)},$$

where the form of $p(\mathbf{z}|\boldsymbol{\omega}, \boldsymbol{\Theta}, \lambda)$ is given by Equation (4). As a result, the normalizing constant in Equation (4) can be canceled out. Note that the last fraction term, which is the proposal density ratio, equals 1 for this random walk Metropolis update on ω_q .

Update of $\boldsymbol{\Theta}$: We update each of $\theta_{qq'}$, $q = 1, \dots, Q-1$, $q' = q, \dots, Q$ by using the DMH algorithm. We first propose a new $\theta_{qq'}^*$ from $N(\theta_{qq'}, \tau_\theta^2)$ and set $\theta_{q'q}^* = \theta_{qq'}^*$ as the matrix is symmetric. Next, according to Equation (5), an auxiliary variable \mathbf{z}^* is simulated via the Gibbs sampler with \mathbf{z} as the starting point. This simulation should be based on the new $\boldsymbol{\Theta}^*$, where all the elements are the same as $\boldsymbol{\Theta}$ except the two elements corresponding to $\theta_{qq'}$ and $\theta_{q'q}$. The proposed value $\theta_{qq'}^*$ as well as $\theta_{q'q}^*$ is then accepted to replace the old values with probability $\min(1, r)$. The Hastings ratio r is given as below:

$$r = \frac{p(\mathbf{z}^*|\boldsymbol{\omega}, \boldsymbol{\Theta}, \lambda)}{p(\mathbf{z}|\boldsymbol{\omega}, \boldsymbol{\Theta}, \lambda)} \frac{p(\mathbf{z}|\boldsymbol{\omega}, \boldsymbol{\Theta}^*, \lambda)}{p(\mathbf{z}^*|\boldsymbol{\omega}, \boldsymbol{\Theta}^*, \lambda)} \frac{N(\theta_{qq'}^*; \mu_\theta, \sigma_\theta^2)}{N(\theta_{qq'}; \mu_\theta, \sigma_\theta^2)} \frac{J(\theta_{qq'}; \theta_{qq'}^*)}{J(\theta_{qq'}^*; \theta_{qq'})},$$

where the form of $\Pr(\mathbf{z}|\boldsymbol{\theta}, \lambda)$ is given by Equation (4). As a result, the normalizing constant in Equation (4) can be canceled out. Note that the last fraction term, which is the proposal density ratio, equals 1 for this random walk Metropolis update on $\theta_{qq'}$.

Update of λ : We update the decay parameter λ by using the DMH algorithm. We first propose a new λ^* from a gamma distribution $\text{Ga}(\lambda^2/\tau_\lambda, \lambda/\tau_\lambda)$, where the mean is λ and the variance is τ_λ . Next, according to Equation (5), we implement the Gibbs sampler to simulate an auxiliary variable \mathbf{z}^* starting from \mathbf{z} based on the new λ^* . The proposed value λ^* is then accepted to replace the old value with probability $\min(1, r)$. The Hastings

ratio r is given as below:

$$r = \frac{p(\mathbf{z}^*|\boldsymbol{\omega}, \boldsymbol{\Theta}, \lambda) p(\mathbf{z}|\boldsymbol{\omega}, \boldsymbol{\Theta}, \lambda^*) \text{Ga}(\lambda^*; a, b) J(\lambda; \lambda^*)}{p(\mathbf{z}|\boldsymbol{\omega}, \boldsymbol{\Theta}, \lambda) p(\mathbf{z}^*|\boldsymbol{\omega}, \boldsymbol{\Theta}, \lambda^*) \text{Ga}(\lambda; a, b) J(\lambda^*; \lambda)},$$

where the form of $\Pr(\mathbf{z}|\boldsymbol{\theta}, \lambda)$ is given by Equation (4). As a result, the normalizing constant in Equation (4) can be canceled out. Note that the last fraction term, which is the proposal density ratio, equals 1 for this random walk Metropolis update on λ .

3.2 Posterior Estimation

We obtain posterior inference by post-processing the MCMC samples after burn-in. Suppose that multiple sequences of MCMC samples,

$$\begin{aligned} &\omega_q^{(1)}, \dots, \omega_q^{(U)}, q = 1, \dots, Q - 1, \\ &\theta_{qq'}^{(1)}, \dots, \theta_{qq'}^{(U)}, q = 1, \dots, Q - 1, q' = q, \dots, Q, \\ &\lambda^{(1)}, \dots, \lambda^{(U)}, \end{aligned}$$

have been collected, where $u, u = 1, \dots, U$ indexes the iteration after burn-in. An approximate Bayesian estimator of each parameter can be simply obtained by averaging over the samples, $\hat{\omega}_q = \sum_{u=1}^U \omega_q^{(u)} / U$, $\hat{\theta}_{qq'} = \sum_{u=1}^U \theta_{qq'}^{(u)} / U$, and $\hat{\lambda} = \sum_{u=1}^U \lambda^{(u)} / U$. For a better understanding of the model, we suggest to project the parameters $(\boldsymbol{\omega}, \boldsymbol{\Theta})$ to $(\boldsymbol{\pi}, \boldsymbol{\Phi})$ according to Equations (6) and (7), or plot the mark interaction functions as given in Equation (8).

4 Simulation

In this section, we use simulated data generated from the proposed model to assess performance of our strategy for posterior inference on the model parameters, $\boldsymbol{\omega}$, $\boldsymbol{\Theta}$, and λ . In

addition, we discuss how to choose the tunable parameter c based on the mark connection function plots and investigate the sensitivity of the proposed model to the choices of c .

We considered to generate the points by using two different point processes: 1) a homogeneous Poisson point process with a constant intensity $\eta = 2000$ over the space $[0, 1]^2$; and 2) a log Gaussian Cox process (LGCP) with an inhomogeneous intensity $\eta(x, y) = \exp(6 + |x - 0.3| + |y - 0.3| + \mathcal{GP}(x, y))$, $x \in [0, 1], y \in [0, 1]$ and \mathcal{GP} denotes a zero-mean Gaussian process with variance equal to 1 and scale equal to 1 (The LGCP setting was also used in Shirota and Gelfand (2016)). We assumed that there are $Q = 2$ different types of points. The mark of each point, z_i , was simulated by using a Gibbs sampler based on Equation (5). We ran 100,000 iterations with a completely random starting configuration of \mathbf{z} . The true parameters were set as follows: 1) the decay parameter $\lambda = 60$ or $\lambda = 0$, and the threshold $c = 0.05$, which implies that any pair of points with distance large than 0.05 were not considered in the model construction; 2) the first-order intensities $\boldsymbol{\omega} = (\omega_1, \omega_2) = (1, 1)$, which correspond to $\boldsymbol{\pi} = (0.5, 0.5)$; and 3) the second-order intensities Θ were set according to each of the five scenarios, as shown in Table 1. They are high/low attraction, complete randomness, and high/low repulsion. *Attraction* is defined as the clustering of points with the same type, while *repulsion* (also known as inhibition or suppression) is defined as the clustering of points with different marks. We repeated the above steps to generate 30 independent datasets for each point process and each setting of λ and Θ . See Figure 3 (a)-(d) for examples of simulated data generated by the homogeneous Poisson process under settings of Θ and $\lambda = 60$. Their corresponding mark connection function (MCF) plots are shown in 3 (i)-(l). MCF is used to describe the spatial correlations of marks, where its quantity $\text{MCF}_{qq'}(d)$ is interpreted as the empirical probability that two points at distance d have marks q and q' . An upward trend in $\text{MCF}_{qq}(d)$ with a downward trend in $\text{MCF}_{qq'}(d)$ indicates attraction, while the opposite case suggests

repulsion.

Table 1: Simulated datasets: The five settings of the second-order intensities Θ and their corresponding Φ .

	High attraction	Low attraction	Complete randomness	Low repulsion	High repulsion
Θ	$\begin{pmatrix} 1.0 & 3.2 \\ 3.2 & 1.0 \end{pmatrix}$	$\begin{pmatrix} 1.0 & 1.9 \\ 1.9 & 1.0 \end{pmatrix}$	$\begin{pmatrix} 1.0 & 1.0 \\ 1.0 & 1.0 \end{pmatrix}$	$\begin{pmatrix} 1.0 & 0.2 \\ 0.2 & 1.0 \end{pmatrix}$	$\begin{pmatrix} 1.0 & -1.2 \\ -1.2 & 1.0 \end{pmatrix}$
Φ	$\begin{pmatrix} 0.9 & 0.1 \\ 0.1 & 0.9 \end{pmatrix}$	$\begin{pmatrix} 0.7 & 0.3 \\ 0.3 & 0.7 \end{pmatrix}$	$\begin{pmatrix} 0.5 & 0.5 \\ 0.5 & 0.5 \end{pmatrix}$	$\begin{pmatrix} 0.3 & 0.7 \\ 0.7 & 0.3 \end{pmatrix}$	$\begin{pmatrix} 0.1 & 0.9 \\ 0.9 & 0.1 \end{pmatrix}$

For the prior on ω_1 , we used a normal distribution $N(1, 1)$, corresponding that $\pi_1 \in [0.125, 0.878]$ with 95% probability *a priori*. For the priors on θ_{11} and θ_{12} , we used a standard normal distribution $N(0, 1)$. Note that we set the constraints $\omega_2 = 1$ and $\theta_{22} = 1$ to avoid the identifiability problem. We set the hyperparameters that control the gamma prior on the exponential decay to $a_\lambda = b_\lambda = 0.001$, which leads to a vague prior with variance equal to 1,000. This is one of the most commonly used weak gamma priors (Gelman et al., 2006). For the tunable parameter c , we chose its true value $c = 0.05$. Results we report below were obtained by running the MCMC chain with 50,000 iterations, discarding the first 50% sweeps as burn in. We started the chain from a model by randomly drawing ω_1 , θ_{11} , θ_{12} , and λ from their prior distributions and assigning a random mark to each z_i . All experiments were implemented in R with Rcpp package to accelerate computations on a Mac PC with 2.60GHz CPU and 16GB memory. In our implementation, the MCMC algorithm ran about 20 minutes for each dataset. We also assessed convergence by using the Raftery-Lewis diagnostic (Raftery and Lewis, 1992), as included in coda package.

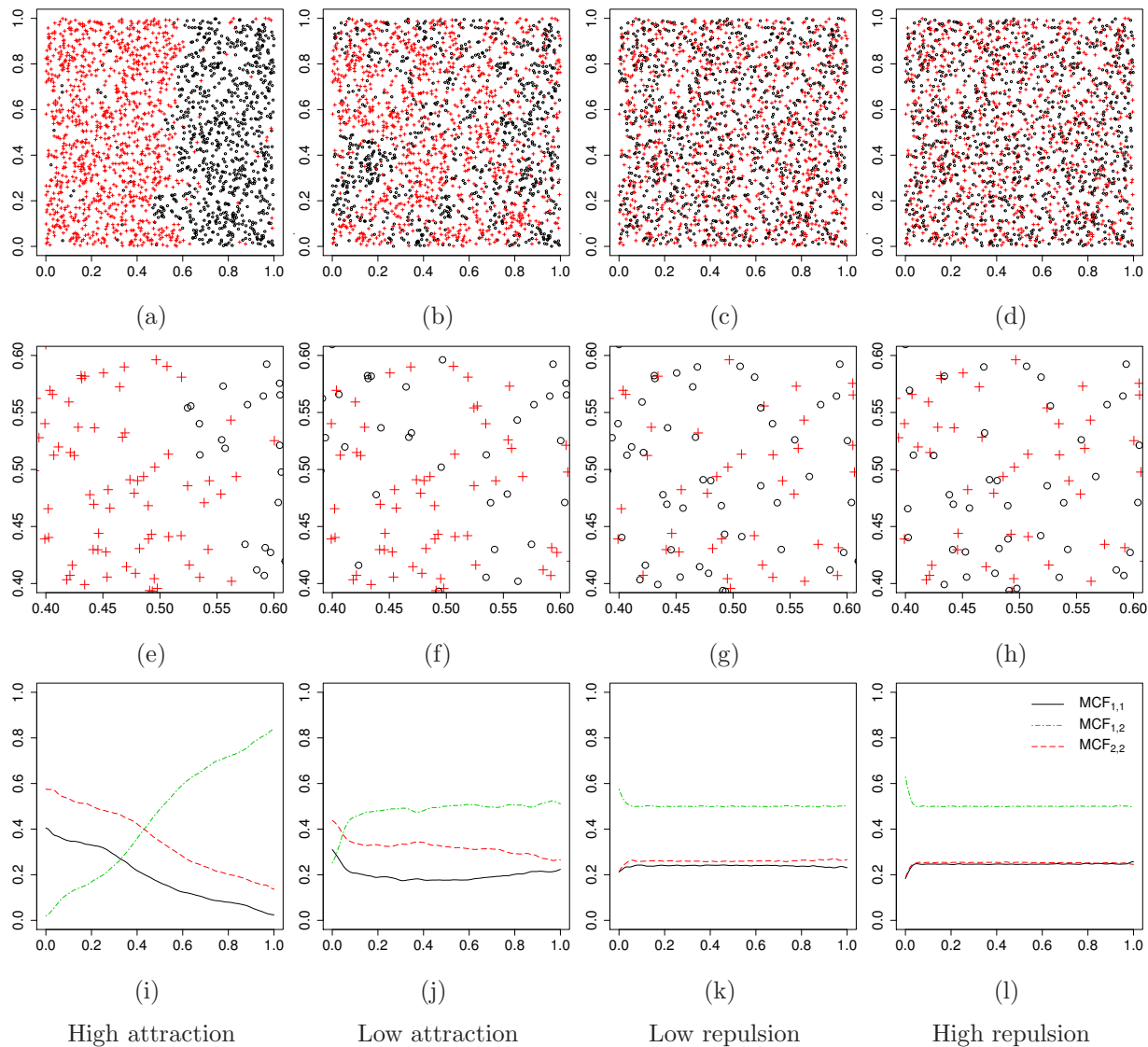


Figure 3: Simulated datasets: (a)-(d): Examples of the generated data from the homogeneous Poisson process with the four scenarios: high/low attraction and high/low repulsion, with $\lambda = 60$. (e)-(h): The center sub-regions of the simulated data as shown in (a)-(d). (i)-(l): The corresponding empirical mark connection function plots.

Tables 2 - 5 summarize the results of posterior inference on the model parameters, under the 20 scenarios (two point process and two settings of λ , and five settings of Θ). Each estimate was obtained by averaging over 30 independent datasets. Overall, the tables indicate that our model fitting strategy based on the DMH algorithm works well, whichever point process is given. However, we notice that the decay parameter λ was greatly overestimated in the complete randomness scenarios. This is not surprising because all z_i 's are completely irrelevant to each other (i.e. $p(z_i = q|\cdot) \propto \exp(-\omega_q)$) under this scenario. Therefore, λ is ill-defined in this situation. The observed large values of λ also indicate the weights, associated with the second-order intensities, decrease faster and thus explain why each mark is dominated by the first-order intensities only. It is also found that the high attraction scenarios had the worst performance on θ_{12} , which measures the interaction strength between different types of points. The reason is that we can only observe a small number of the interacting pairs between type 1 and 2 points. Take Figure 3 (a) for example, such interacting pairs can be only seen near the border between the two clumps. Therefore, we may expect a biased estimation on θ_{12} .

The proposed model contains one tunable parameter c , which defines the neighborhood for each point. A large value of c quadratically increases the computational cost, while a small value may cause biased estimates. We suggest users choose a value of 0.1 or less unless there is strong evidence in support of a larger value. Such evidence could be either subjective, such as an assessment from an experienced expert, or objective, such as MCF plots from the data (e.g. Figure 3 (i)-(l)). For repulsion scenarios, it is found that the MCF curve converges right after d passing over the true value of c . Thus, we could choose c based on such an observation. However, for attraction scenarios, the curve tends to have a much bigger lag, especially for larger values of ϕ_{12} or ϕ_{21} . In this case, we suggest users choose $c = 0.1$. We also conducted a sensitivity analysis to the specification of c . We fit each of

Table 2: Simulated datasets from the homogeneous Poisson process with $\lambda = 60$: Results of posterior inference on the model parameters. Values are averaged over 30 simulated datasets for each scenario, with standard deviations indicated in parentheses.

	High attraction	Low attraction	Complete randomness	Low repulsion	High repulsion
ω_1	1.0	1.0	1.0	1.0	1.0
$\hat{\omega}_1$	1.30(0.39)	1.05(0.12)	1.04(0.09)	1.08(0.18)	1.05(0.19)
θ_{11}	1.0	1.0	1.0	1.0	1.0
$\hat{\theta}_{11}$	0.71(0.37)	0.97(0.09)	0.84(0.33)	0.94(0.15)	0.95(0.14)
θ_{12}	3.2	1.9	1.0	0.2	-1.2
$\hat{\theta}_{12}$	2.52(0.26)	1.82(0.17)	0.81(0.30)	0.05(0.19)	-1.14(0.20)
λ	60	60	60	60	60
$\hat{\lambda}$	48.36(6.79)	58.77(7.49)	186.76(118.09)	65.58(11.82)	58.75(4.81)

Table 3: Simulated datasets from the homogeneous Poisson process with $\lambda = 0$: Results of posterior inference on the model parameters. Values are averaged over 30 simulated datasets for each scenario, with standard deviations indicated in parentheses.

	High attraction	Low attraction	Complete randomness	Low repulsion	High repulsion
ω_1	1.0	1.0	1.0	1.0	1.0
$\hat{\omega}_1$	1.31(0.26)	1.19(0.54)	1.04(0.07)	1.01(0.26)	0.97(0.43)
θ_{11}	1.0	1.0	1.0	1.0	1.0
$\hat{\theta}_{11}$	0.89(0.10)	0.91(0.14)	0.77(0.38)	1.00(0.04)	0.99(0.15)
θ_{12}	3.2	1.9	1.0	0.2	-1.2
$\hat{\theta}_{12}$	2.66(0.13)	2.00(0.16)	0.73(0.34)	0.11(0.05)	-1.07(1.15)
λ	0	0	0	0	0
$\hat{\lambda}$	1.74(0.58)	2.74(1.15)	234.21(135.37)	0.57(0.42)	6.93(35.36)

Table 4: Simulated datasets from the LGCP process with $\lambda = 60$: Results of posterior inference on the model parameters. Values are averaged over 30 simulated datasets for each scenario, with standard deviations indicated in parentheses.

	High attraction	Low attraction	Complete randomness	Low repulsion	High repulsion
ω_1	1.0	1.0	1.0	1.0	1.0
$\hat{\omega}_1$	1.05(0.14)	1.02(0.09)	1.04(0.10)	1.00(0.13)	0.98(0.14)
θ_{11}	1.0	1.0	1.0	1.0	1.0
$\hat{\theta}_{11}$	0.87(0.26)	0.87(0.30)	0.61(0.50)	0.91(0.31)	0.96(0.22)
θ_{12}	3.2	1.9	1.0	0.2	-1.2
$\hat{\theta}_{12}$	2.64(0.48)	1.75(0.22)	0.63(0.40)	-0.07(0.33)	-1.20(0.31)
λ	60	60	60	60	60
$\hat{\lambda}$	48.29(12.63)	61.11(22.04)	194.14(119.57)	75.70(32.85)	60.758(9.23)

Table 5: Simulated datasets from the LGCP process with $\lambda = 0$: Results of posterior inference on the model parameters. Values are averaged over 30 simulated datasets for each scenario, with standard deviations indicated in parentheses.

	High attraction	Low attraction	Complete randomness	Low repulsion	High repulsion
ω_1	1.0	1.0	1.0	1.0	1.0
$\hat{\omega}_1$	1.12(0.26)	1.05(0.28)	1.04(0.09)	1.00(0.20)	0.98(0.24)
θ_{11}	1.0	1.0	1.0	1.0	1.0
$\hat{\theta}_{11}$	0.80(0.31)	0.91(0.17)	0.57(0.52)	0.99(0.10)	1.01(0.11)
θ_{12}	3.2	1.9	1.0	0.2	-1.2
$\hat{\theta}_{12}$	3.01(0.25)	1.91(0.12)	0.60(0.43)	0.05(0.17)	-1.35(0.22)
λ	0	0	0	0	0
$\hat{\lambda}$	1.00(0.47)	2.28(1.16)	208.17(107.95)	1.49(1.89)	0.67(0.51)

the 120 simulated datasets generated from the homogeneous Poisson process (30 for each scenario, excluding the complete randomness one) into the proposed model with $c = 0.03$, 0.05 , and 0.1 , respectively. Figure 4 (a)-(d) show the boxplots of the three estimates $\hat{\omega}_1$, $\hat{\theta}_{11}$, and $\hat{\theta}_{12}$ under different values of c for each scenario. As we can see, the model was quite robust to different choices of c .

5 Application

In this section, we first investigate the performance of our methodology using three benchmark datasets in the R package `spatstat`, which is a major tool for spatial point pattern analysis. The proposed model is then applied to a large cohort of lung cancer pathology images, and it reveals novel potential imaging biomarkers for lung cancer prognosis.

5.1 `spatstat` Datasets

One of the basic data types offered by `spatstat` is multi-type point pattern data. We use two retinal cell datasets with marks on/off and one wood dataset with six species to quantify their attraction/repulsion characteristics by using the proposed model.

Since 1970s, there has been considerable interest in studying the spatial pattern presented by particular types of mammalian retinal cell bodies (Wässle and Riemann, 1978; Wässle et al., 1978; Wässle and Illing, 1981; Wässle and Peichl, 1981; Wässle et al., 1981; Hughes, 1981a,b; Peichl and Wässle, 1981; Vaney et al., 1981; Rockhill et al., 2000). One of the two commonly used examples is the `amacrine` cells dataset (Diggle, 1986), consisting of two types (i.e. on/off) of displaced amacrine cells within the retinal ganglion cell layer of a rabbit. The other is the `betacells` dataset (Wässle and Illing, 1981), composed of two types (i.e. on/off) beta cells that are associated with the resolution of fine details in

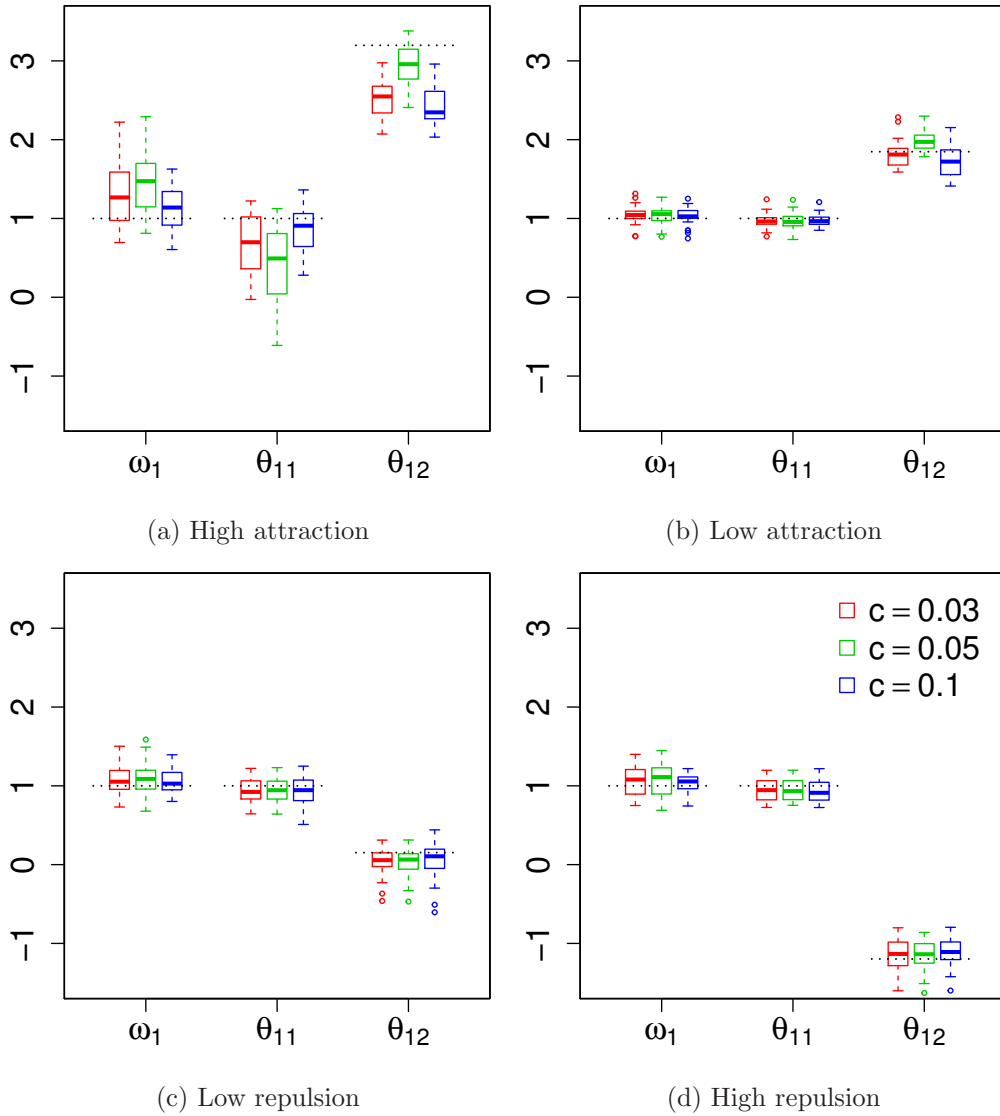


Figure 4: Simulated datasets: The boxplots of $\hat{\omega}_1$, $\hat{\theta}_{11}$, and $\hat{\theta}_{12}$ under different choices of c for each scenario: (a) high attraction, (b) low attraction, (c) low repulsion, and (d) high repulsion scenarios, with the black dashed lines indicating the true values.

the visual system of a cat. Figure 5 (a) depicts how the two different types of amacrine cells distribute in a $1070 \times 600\mu\text{m}$ rectangular region, where the 142 circles (\circ) represent those cells processing “light-off” information and the 152 crosses ($+$) represent those cells processing “light-on” information. Figure 6 (a) shows the cell distribution map of the `betacells` dataset in an approximate $753 \times 1,000\mu\text{m}$ rectangular window, where the 70 circles (\circ) represent those “off” beta cells and the 65 crosses ($+$) represent those “on” beta cells. Their mark connection function plots are shown in Figure 5 (b) and Figure 6 (b), respectively. Although both of the plots clearly indicate strong repulsion among cells with the same type and the interaction region radius around 0.1, no quantities can be accurately estimated further.

For each dataset, we applied the proposed model with the same hyperparameter and algorithm settings as described in Section 4 and the choice of $c = 0.2$. We ran four independent MCMC chains with 50,000 iterations, discarding the first half as burn-in. The Gelman and Rubin’s convergence diagnostics Gelman and Rubin (1992) were used to inspect the convergence. Those statistics for all the model parameters were below 1.03, ranging from 1.002 to 1.029, clearly suggesting that the MCMC chains were run for a sufficient number of iterations. Then, for each dataset, we pooled together the outputs from the four chains and report the results as below. For dataset `amacrine`, we obtained the decay $\hat{\lambda} = 30.195$, the first-order intensity $\hat{\omega}_{\text{off}} = 0.85$ corresponding to $\hat{\pi}_{\text{off}} = 0.538$ and $\hat{\pi}_{\text{on}} = 0.462$, and the second-order intensities $\hat{\theta}_{\text{off,off}} = 0.35$ and $\hat{\theta}_{\text{on,off}} = \hat{\theta}_{\text{off,on}} = -4.024$ corresponding to $\hat{\phi}_{\text{off,off}} = 0.012$, $\hat{\phi}_{\text{on,off}} = 0.999$, $\hat{\phi}_{\text{off,on}} = 0.993$, and $\hat{\phi}_{\text{on,on}} = 0.007$. For dataset `betacells`, we obtained the decay $\hat{\lambda} = 15.695$, the first-order intensity $\hat{\omega}_{\text{off}} = 0.882$ corresponding to $\hat{\pi}_{\text{off}} = 0.53$ and $\hat{\pi}_{\text{on}} = 0.47$, and the second-order intensities $\hat{\theta}_{\text{off,off}} = 0.65$ and $\hat{\theta}_{\text{on,off}} = \hat{\theta}_{\text{off,on}} = -3.104$ corresponding to $\hat{\phi}_{\text{off,off}} = 0.023$, $\hat{\phi}_{\text{on,off}} = 0.977$, $\hat{\phi}_{\text{off,on}} = 0.984$, and $\hat{\phi}_{\text{on,on}} = 0.016$. Figure 5 (c) and Figure 6 (c) also show the levelplot of the estimated

$\hat{\phi}$ and the 95% credible interval for each $\hat{\phi}_{qq'}$. Figure 5 (d) and Figure 6 (d) plots the mark interaction functions according to the estimated model parameters. Our method, as well as other methods (Diggle, 1986; Van Lieshout and Baddeley, 1999), suggest repulsion between the cells (e.g. most cells have a nearest neighbor of the opposite type). The message about oppositely labelled pairs between neighbor cells would strengthens the assumption that there are two separate channels for brightness and darkness as postulated by Hering in 1874. Indeed, we provide an accurate quantitative description ω and Θ , along with the corresponding probability measurements π and Φ , which may benefit the development and retinal sampling efficiency.

The third dataset in `spatstat` that was used to demonstrate the proposed model is the `lansing` dataset. It contains the locations and botanical classification of trees in Lansing Woods, Clinton County, Michigan, United States. Gerrard (1969) investigated $n = 2,251$ trees, including 135 black oaks (\circ), 703 hickories ($+$), 514 maples (\triangle), 105 miscellaneous trees (\times), 346 red oaks (\square), and 448 white oaks ($*$), over an area of 924×924 feet (19.6 acre). Figure 7 (a) shows the rescaled multivariate spatial pattern that consists of $Q = 6$ types of trees in the unit square, where each shape/color represents a tree category. Next, Figure 7 (b) plots the corresponding mark connection functions between the same mark, which indicate exhibition of clustering among the trees with the same type.

We applied the proposed model with the same hyperparameter and algorithm settings as described in Section 4 and the choice of $c = 0.1$. Again, we ran four independent MCMC chains with 50,000 iterations and assessed the convergence by the Gelman and Rubin’s convergence diagnostics. Those statistics for all parameters range from 1.003 to 1.022. Results we report here were obtained by pooling together the outputs from the four chains. We obtained the decay $\hat{\lambda} = 49.764$, the first-order intensities $\hat{\omega}_{\text{black oak}} = 2.514$, $\hat{\omega}_{\text{hickory}} = 1.315$, $\hat{\omega}_{\text{maple}} = 1.654$, $\hat{\omega}_{\text{misc}} = 3.104$, and $\hat{\omega}_{\text{red oak}} = 2.016$, corresponding to

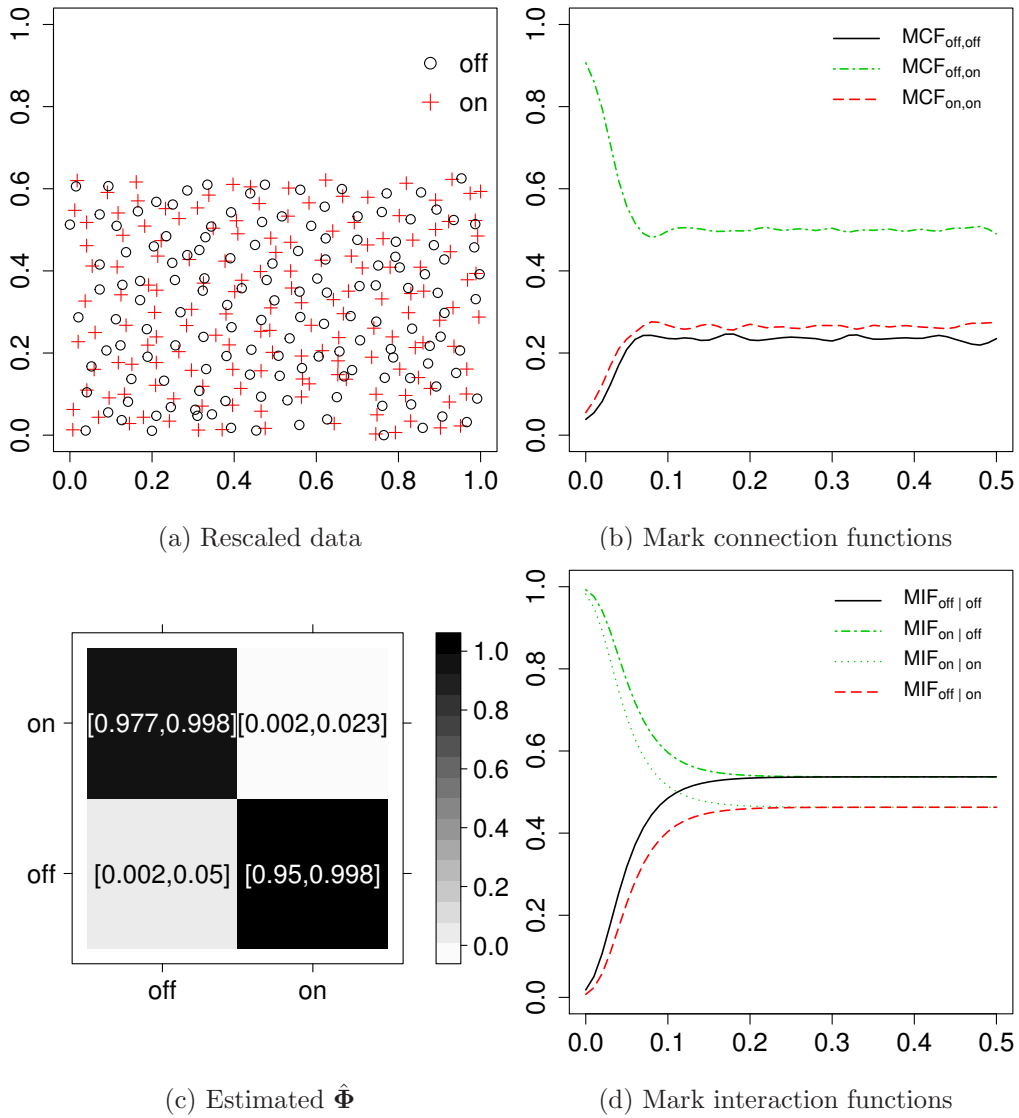


Figure 5: amacrine dataset: (a) The rescaled marked point data, with a unit standing for approximate $1,000\mu\text{m}$; (b) The empirical mark connection function plots; (c) The levelplot of the estimated $\hat{\phi}$, with the numbers in square brackets giving the 95% credible interval; (d) The estimated mark interaction function plots.

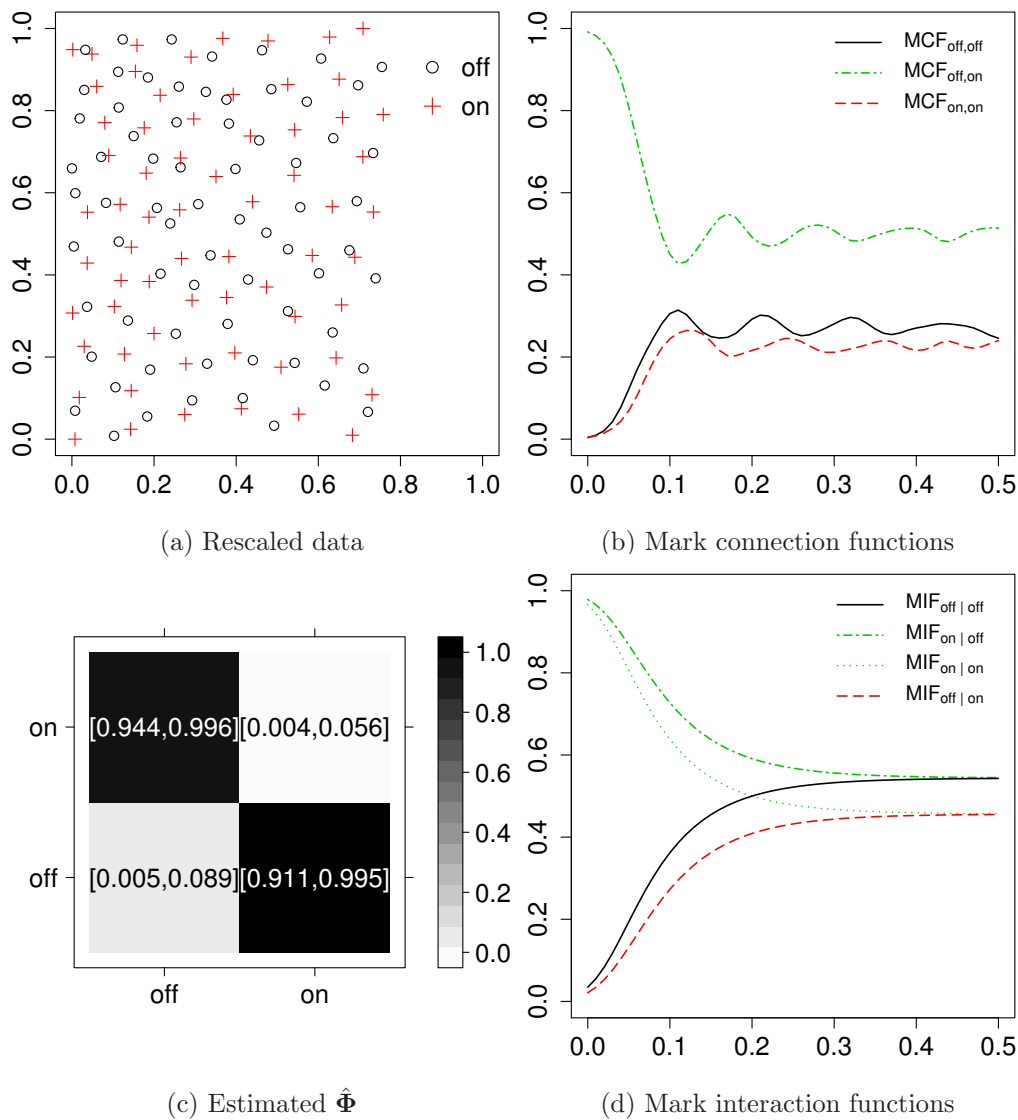


Figure 6: betace11s dataset: (a) The rescaled marked point data, with a unit standing for approximate $1,000\mu\text{m}$; (b) The empirical mark connection function plots; (c) The levelplot of the estimated $\hat{\phi}$, with the numbers in square brackets giving the 95% credible interval; (d) The estimated mark interaction function plots.

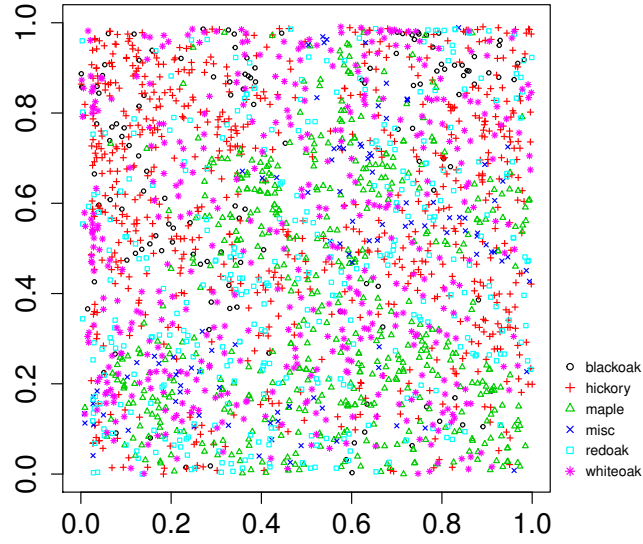
$\hat{\pi}_{\text{black oak}} = 0.074$, $\hat{\pi}_{\text{hickory}} = 0.247$, $\hat{\pi}_{\text{maple}} = 0.176$, $\hat{\pi}_{\text{misc}} = 0.041$, $\hat{\pi}_{\text{red oak}} = 0.123$, and $\hat{\pi}_{\text{white oak}} = 0.339$. The estimated Θ is given as below

$$\hat{\Theta} = \begin{matrix} & \text{black oak} & \text{hickory} & \text{maple} & \text{misc} & \text{red oak} & \text{white oak} \\ \begin{matrix} \text{black oak} \\ \text{hickory} \\ \text{maple} \\ \text{misc} \\ \text{red oak} \\ \text{white oak} \end{matrix} & \left(\begin{matrix} -0.066 & 0.978 & 1.449 & 3.836 & 0.970 & 0.997 \\ 0.978 & 0.570 & 1.332 & 1.166 & 1.003 & 1.200 \\ 1.449 & 1.332 & 0.495 & 0.955 & 1.108 & 1.202 \\ 3.836 & 1.166 & 0.955 & -0.092 & 1.044 & 1.187 \\ 0.970 & 1.003 & 1.108 & 1.044 & 0.535 & 1.266 \\ 0.997 & 1.200 & 1.202 & 1.187 & 1.266 & 1.000 \end{matrix} \right) \end{matrix}$$

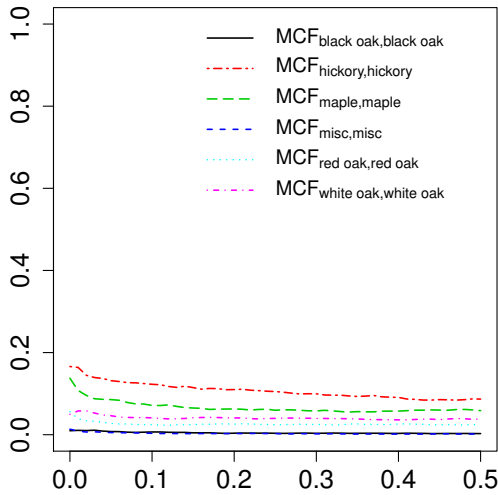
, and the corresponding $\hat{\Phi}$ is shown in Figure 8 with the 95% credible interval for each parameter. The pattern reveals that the first five types of trees exhibits clustering, especially for black oak and miscellaneous trees. This means if one species has a clump in an area, then no other species tends to form a clump in the same location. We also found white oak has the least $\hat{\phi}_{qq}$ value, which suggests its spatial pattern is more likely random. Those findings were also reported in Cox and Lewis (1976) and Cox (1979). In addition, our method outputs the mark interaction functions between the same mark, as shown in Figure 7 (c), indicating there is no interaction between the same type trees beyond about 90 feet.

5.2 Case Study on Lung Cancer

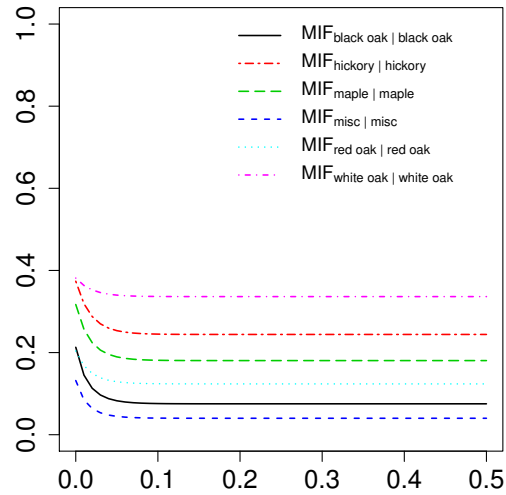
Lung cancer is the leading cause of death from cancer in both men and women. Non-small-cell lung cancer (NSCLC) accounts for about 85% of deaths from lung cancer. Current guidelines for diagnosing and treating NSCLC are largely based on pathological examination of H&E-stained tumor tissue section slides. We have developed a ConvPath pipeline



(a) Rescaled data



(b) Mark connection functions



(c) Mark interaction functions

Figure 7: `lansing` dataset: (a) The rescaled marked point data, with a unit standing for approximate 282m (≈ 924 ft); (b) The empirical mark connection function plots (only the MCFs between the same mark are shown); (c) The estimated mark interaction function plots (only the MIFs between the same mark are shown).

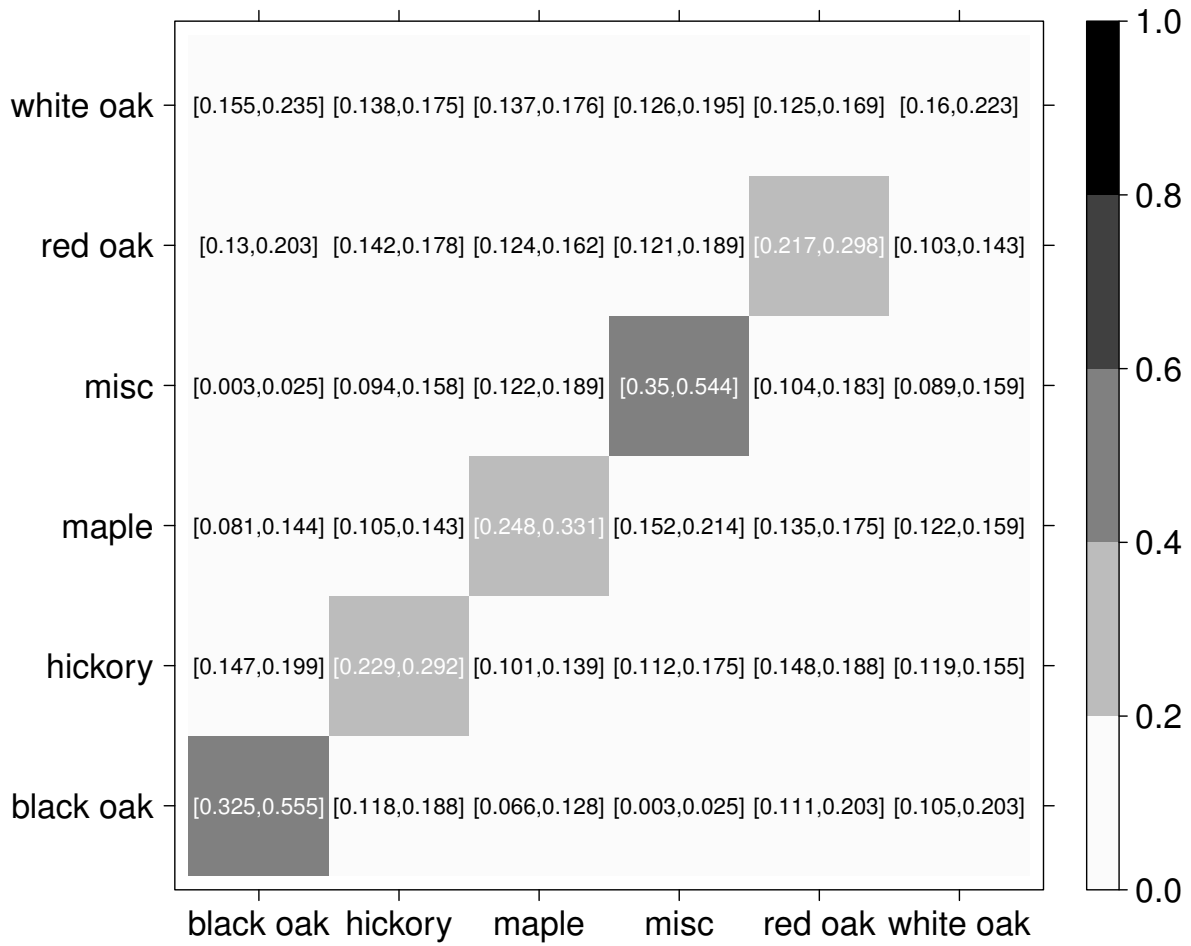


Figure 8: lansing dataset: The levelplot of the estimated $\hat{\phi}$, with the numbers in square brackets giving the 95% credible interval.

(<https://qbrc.swmed.edu/projects/cnn/>) to determine the locations and types of cells observed in the processed tumor pathology images. Specifically, the classifier, based on a convolutional neural network (CNN), was trained using a large cohort of lung cancer pathology images manually labelled by pathologists, and it can classify each cell by its $Q = 3$ category: lymphocyte (a type of immune cell), stromal, or tumor cell.

In this case study, we used the pathology images from 188 NSCLC patients in the National Lung Screening Trial (NLST). Each patient has one or more tissue slide(s) scanned at 40x magnification. The median size of the slides is $24,244 \times 19,261$ pixels. A lung cancer pathologist first determined and labeled the region of interest (ROI) within the tumor region(s) from each tissue slide using an annotation tool, ImageScope (Leica Biosystem). ROIs are regions of the slides containing the majority of the malignant tissues and are representative of the whole slide image. Then we randomly chose five square regions, each of which is in a 5000×5000 pixel window, per ROI as the sample images. The total number of sample images that we collected was 1,585. For each sample image, the ConvPath software was used to identify cells from the sample images and classify each cell into one of three types, so that a corresponding spatial map of cells was generated and used as the input of our model. The number of cells in each sample image ranges from $n = 2,876$ to 26,463. Figure 9 (a) and (b) show the examples of two sample images and Figure 10 displays the mark connection functions of the whole datasets, which exhibits attraction (i.e. the cells with the same type tend to cluster).

We applied the proposed model with the same hyperparameter and algorithm settings as described in Section 4 and different choices of $c = 0.02$, $c = 0.05$, and $c = 0.1$. We then computed the pairwise Pearson correlation coefficients between the estimated model parameters under different choices of c . These correlations indicated substantial agreement between any pair of settings, with values ranging from 0.967 to 0.997. Results we report

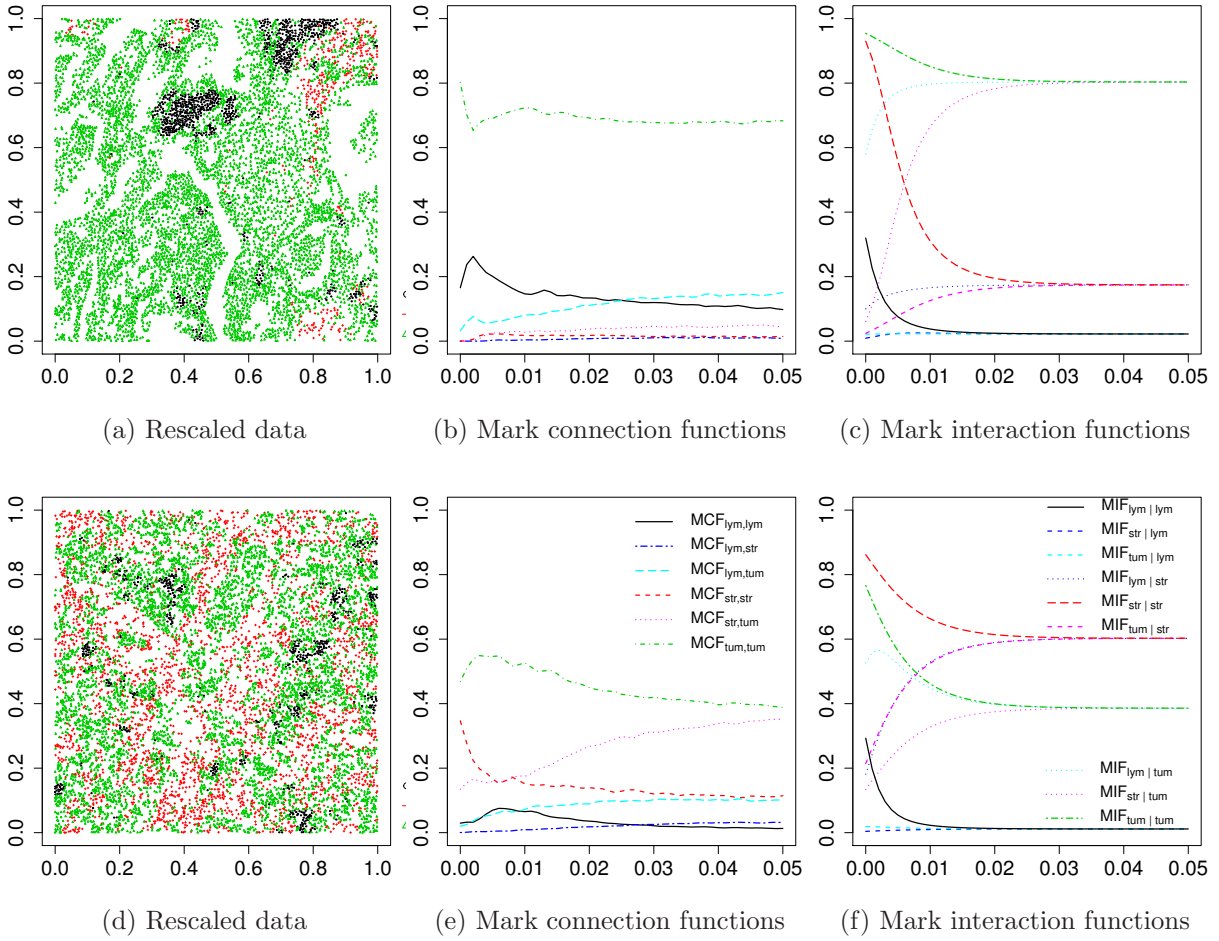


Figure 9: Lung cancer case study: (a) and (d) Two examples of the rescaled marked point data from NLST dataset, where black, red, and green points represent lymphocyte, stromal, and green cells; (b) and (e) The empirical mark connection function plots; (c) and (f) The estimated mark interaction function plots. For the data shown in (a), $\hat{\lambda} = 172.102$, $\hat{\pi}_{\text{lym}} = 0.022$, $\hat{\pi}_{\text{str}} = 0.173$, $\hat{\pi}_{\text{tum}} = 0.805$, and $\hat{\phi}_{\text{tum, str}} = 0.012$; For the data shown in (d), $\hat{\lambda} = 169.268$, $\hat{\pi}_{\text{lym}} = 0.011$, $\hat{\pi}_{\text{str}} = 0.603$, $\hat{\pi}_{\text{tum}} = 0.386$, and $\hat{\phi}_{\text{tum, str}} = 0.162$

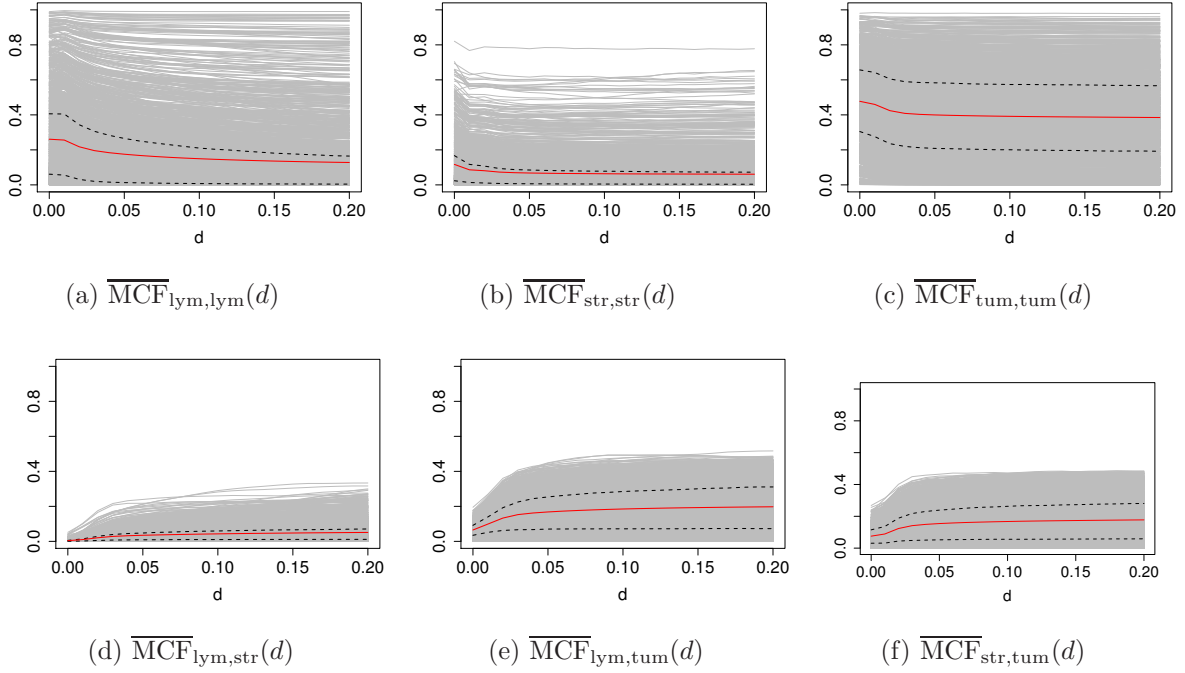


Figure 10: Lung cancer case study: The empirical mark connection function plots between marks: (a) lymphocyte and lymphocyte, (b) stromal and stromal, (c) tumor and tumor, (d) lymphocyte and stromal, (e) lymphocyte and tumor, and (f) stromal and tumor. Each grey line represents one of the 1,585 sample images. Red solid lines indicate the MCF means against the distance d .

below were obtained by using the estimated parameters under the choice of $c = 0.1$.

With the estimated parameters in each sample image, we conducted a downstream analysis to investigate their associations with the other measurements of interest. Specifically, a Cox proportional hazards model (Cox, 1992) was fitted to evaluate the association between the transformed model parameters $\hat{\boldsymbol{\pi}}$ and $\hat{\boldsymbol{\Phi}}$, and patient survival outcomes, after adjusting for other clinical information, such as age, gender and tobacco history. Multiple sample images from the same patient were modeled as correlated observations in the Cox regression model to compute a robust variance for each coefficient. The overall P -value for the Cox model is 0.0021 (Wald test), and the P -value and coefficient for each individual variable are summarized in Table 6. The results imply that a low interaction between stromal and tumor cells ($\phi_{\text{tum, str}}$) is associated with good prognosis in NSCLC patients (P -value=0.0073). Interestingly, Beck et al. (2011) also discovered that the morphological features of the stroma in the tumor region are associated with patient survival in a systematic analysis of breast cancer. Besides, the abundance of the stromal cells itself (P -value=0.017) is also a prognostic factor, while the underlying biological mechanism is currently unknown. The positive coefficient of the predictor $\phi_{\text{tum, str}}$ implies that a higher value may reveal a higher risk of death. Indeed, we obtained $\hat{\phi}_{\text{tum, str}} = 0.012$ for the data shown in Figure 9(a) and it is from a patient who was still alive over 2,615 days after the surgery, while the estimated value of $\phi_{\text{tum, str}} = 0.162$ for the data shown in Figure 9(d) and it is from a patient died on the 1,246th days after the surgery. These two images have distinctive patterns, as the former clearly shows the same type cells tend to clump in the same area, while the latter displays a case where stromal and tumor cells are thoroughly mixed together, indicating the spread of stromal cells into the tumor region. Although the high/low interaction between stromal and tumor cells can be easily seen by eyes in these two images, the patterns are much more subtle for many other images. Therefore, the

proposed model can be used to predict the survival time when human visualization does not work.

Furthermore, we performed a model-based clustering analysis on the features extracted by the model. First, each of the eight parameters $\hat{\phi}_{\text{str,lym}}$, $\hat{\phi}_{\text{tum,lym}}$, $\hat{\phi}_{\text{lym,str}}$, $\hat{\phi}_{\text{tum,str}}$, $\hat{\phi}_{\text{lym,tum}}$, $\hat{\phi}_{\text{str,tum}}$, $\hat{\pi}_{\text{lym}}$, $\hat{\pi}_{\text{str}}$ of multiple sample images from the same patient were averaged. We then used the multivariate Gaussian mixture model (Fraley and Raftery, 2002) to cluster patients using those 8 parameter. This was done using R package `mclust`. To estimate the number of clusters that best represents the data as well as its covariance structure, we plotted the Bayesian information criterion (BIC) values against the number of clusters from 1 to 9, as shown in Figure 11 (a). It shows that clustering patients into three groups achieves the best fit of the data measured by BIC, where the first (in black), second (in red), and third (in green) groups have 79, 77, and 32 patients, respectively. Next, we visualized the means of these patient-level parameters for each group, shown as a radar chart in Figure 11 (b), and plotted the Kaplan-Meier survival curve for each group in Figure 11 (c). The patients from group 1 had higher survival probabilities, while the patients from the last group had the poor prognosis. The log-rank test shows that there are significant differences (P -value= 0.024) among the survival curves of the three groups. The analysis, again, demonstrated that the proposed mark interaction features can be used as a potential biomarker for patient prognosis.

By contrast, we fitted a similar Cox regression model by using the mark connection function features as predictors. Specifically, we first used $\text{MCF}_{\text{lym,str}}(d)$, $\text{MCF}_{\text{lym,tum}}(d)$, and $\text{MCF}_{\text{str,tum}}(d)$, where $d = 0.1$ for each sample image as covariates. The results are summarized in Table 7. As we can see, there is no significant predictor and the overall P -value for the Cox model is 0.47 (Wald test). Then, we tried to vary the value of d from 0 to 0.2, Figure 10 shows the P -values of $\text{MCF}_{\text{lym,str}}(d)$, $\text{MCF}_{\text{lym,tum}}(d)$, and $\text{MCF}_{\text{str,tum}}(d)$

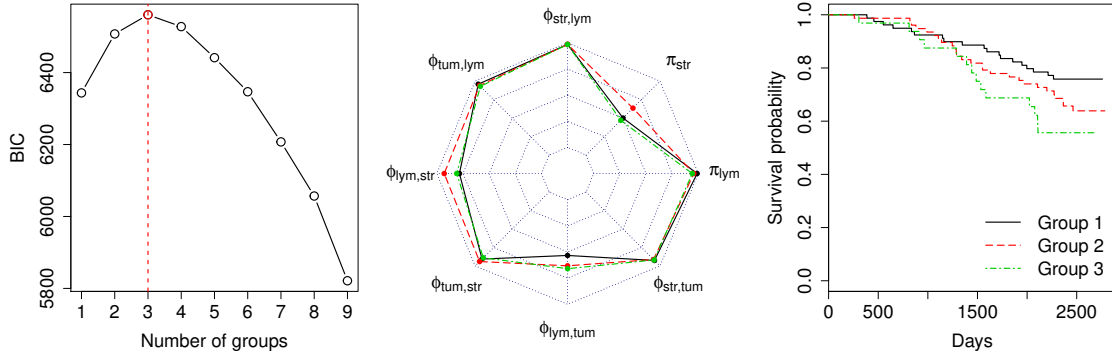


Figure 11: Lung cancer case study: (a) The BIC plot of the model-based clustering on the patient-level parameters $(\hat{\phi}_{str,lym}, \hat{\phi}_{tum,lym}, \hat{\phi}_{lym,str}, \hat{\phi}_{tum,str}, \hat{\phi}_{lym,tum}, \hat{\phi}_{str,tum}, \hat{\pi}_{lym}, \hat{\pi}_{str})$; (b) The radar chart of the averaged patient-level parameters of the three groups (shown in different colors), where the outer ring and the center have the values of 0 and 1, respectively; (c) The Kaplan-Meier plot for the three groups with patient survival.

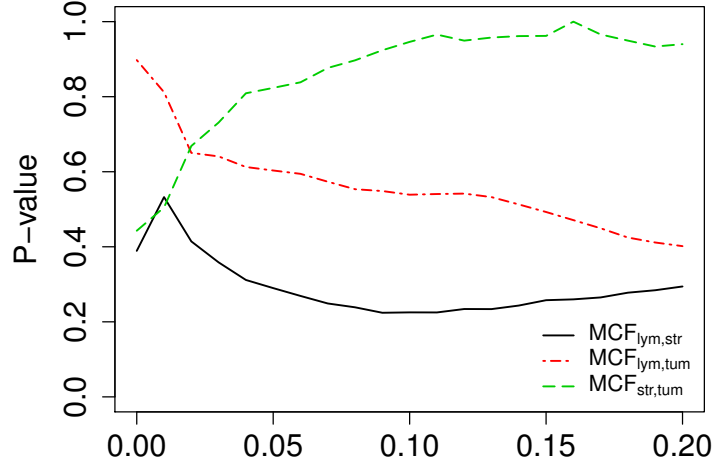


Figure 12: Lung cancer case study: The P -values of $\text{MCF}_{\text{lym, str}}(d)$, $\text{MCF}_{\text{lym, tum}}(d)$, and $\text{MCF}_{\text{str, tum}}(d)$ under different choices of d by fitting Cox regression models with survival time and vital status as responses, and $\text{MCF}_{\text{lym, str}}(d)$, $\text{MCF}_{\text{lym, tum}}(d)$, $\text{MCF}_{\text{str, tum}}(d)$, proportion of lymphocyte cells, proportion of stromal cells, gender, and smoking history as predictors.

against d . Again, we were unable to find any association between cell-cell interactions and clinical outcomes. The comparison demonstrates the advantage of modeling the pathology images via the proposed model over the traditional methods for characterizing spatial correlation.

6 Conclusion

The major cell types in a malignant tissue of lung are tumor cells, stromal cells and infiltrating lymphocytes. The distribution of different types of cells and their interactions play

a key role in tumor progression and metastasis. For example, stromal cells are connective tissue cells such as fibroblasts and pericytes, and their interaction with tumor cells is known to play a major role in cancer progression (Wiseman and Werb, 2002). Tumor-infiltrating lymphocytes have been associated with patient prognosis in multiple tumor types previously (Huh et al., 2012; Brambilla et al., 2016). Recent advances in deep learning methods have made possible the automatic identification and classification of cells at large scale. For example, the ConvPath pipeline could determine the location and cell type for thousands of cells. However, it is challenging to utilize the vast amount of information extracted digitally. In this study, we developed a rigorous statistical method to model the spatial interaction among different types of cells in tumor regions. We focused on modeling the spatial correlation of marks in a spatial pattern that arose from a pathology image study. A Bayesian framework was proposed in order to model how the mark in a pattern might have been formed given the points. The proposed model can utilize the spatial information of thousands of points from any point processes. The output of the model is the parameters that characterize the spatial pattern. After a certain transformation, the parameters are identifiable and interpretable, and most importantly, transferable for conducting an association study with other measurements of interest. Furthermore, this statistical methodology provides new insights into the biological mechanisms of cancer.

For the lung cancer pathology imaging data, our study shows the interaction strength between stromal and tumor cells is significantly associated with patient prognosis. This parameter can be easily measured using the proposed method and used as a potential biomarker for patient prognosis. This biomarker can be translated into real clinical tools at low cost because it is based only on tumor pathology slides, which are available in standard clinical care.

Several extensions of our model are worth investigating. First, the proposed model can

be extended to finite mixture models for inhomogeneous mark interactions. Second, the correlation among first- and second-order intensity parameters could be taken into account by modeling them as a multivariate normal distribution. Last but not least, the proposed model provides a good chance to investigate the performance of other approximate Bayesian computation methods. These could be future research directions.

References

- Mitval B Amin, Pheroze Tamboli, Shakil H Merchant, Nelson G Ordóñez, Jungsil Ro, Alberto G Ayala, and Jae Y Ro. Micropapillary component in lung adenocarcinoma: a distinctive histologic feature with possible prognostic significance. *The American Journal of Surgical Pathology*, 26(3):358–364, 2002.
- George Avalos and Francesca Bucci. Exponential decay properties of a mathematical model for a certain fluid-structure interaction. In *New Prospects in Direct, Inverse and Control Problems for Evolution Equations*, pages 49–78. Springer, 2014.
- Justine A Barletta, Beow Y Yeap, and Lucian R Chirieac. Prognostic significance of grading in lung adenocarcinoma. *Cancer*, 116(3):659–669, 2010.
- Andrew H Beck, Ankur R Sangoi, Samuel Leung, Robert J Marinelli, Torsten O Nielsen, Marc J van de Vijver, Robert B West, Matt van de Rijn, and Daphne Koller. Systematic analysis of breast cancer morphology uncovers stromal features associated with survival. *Science Translational Medicine*, 3(108):108ra113, 2011.
- Julian E Besag. Comment on ‘modelling spatial patterns’. *Journal of the Royal Statistical Society. Series B (Methodological)*, 39:193–195, 1977.

- Alain C Borczuk, Fang Qian, Angeliki Kazeros, Jennifer Eleazar, Adel Assaad, Joshua R Sonett, Mark Ginsburg, Lyall Gorenstein, and Charles A Powell. Invasive size is an independent predictor of survival in pulmonary adenocarcinoma. *The American Journal of Surgical Pathology*, 33(3):462, 2009.
- Elisabeth Brambilla, Gwénaél Le Teuff, Sophie Marguet, Sylvie Lantuejoul, Ariane Dunant, Stephen Graziano, Robert Pirker, Jean-Yves Douillard, Thierry Le Chevalier, Martin Filipits, et al. Prognostic effect of tumor lymphocytic infiltration in resectable non-small-cell lung cancer. *Journal of Clinical Oncology*, 34(11):1223–1230, 2016.
- Victor Chulaevsky. Exponential decay of eigenfunctions in a continuous multi-particle anderson model with sub-exponentially decaying interaction. *arXiv preprint arXiv:1408.4646*, 2014.
- David R Cox. Regression models and life-tables. In *Breakthroughs in Statistics*, pages 527–541. Springer, 1992.
- Trevor F Cox. A method for mapping the dense and sparse regions of a forest stand. *Applied Statistics*, pages 14–19, 1979.
- Trevor F Cox and Toby Lewis. A conditioned distance ratio method for analyzing spatial patterns. *Biometrika*, 63(3):483–491, 1976.
- Mark RT Dale. *Spatial pattern analysis in plant ecology*. Cambridge University Press, 2000.
- Peter J Diggle. Displaced amacrine cells in the retina of a rabbit: analysis of a bivariate spatial point pattern. *Journal of Neuroscience Methods*, 18(1-2):115–125, 1986.
- Peter J Diggle and Robin K Milne. Bivariate Cox processes: some models for bivariate

- spatial point patterns. *Journal of the Royal Statistical Society. Series B (Methodological)*, pages 11–21, 1983.
- Peter J Diggle, Stephen J Eglén, and John B Troy. Modelling the bivariate spatial distribution of amacrine cells. *Case Studies in Spatial Point Process Modeling*, pages 215–233, 2006.
- PJ Diggle and TF Cox. On sparse sampling methods and tests of independence for multivariate spatial point patterns. *Bulletin of the International Statistical Institute*, 49: 213–229, 1981.
- Chris Fraley and Adrian E Raftery. Model-based clustering, discriminant analysis, and density estimation. *Journal of the American statistical Association*, 97(458):611–631, 2002.
- Andrew Gelman and Donald B Rubin. Inference from iterative simulation using multiple sequences. *Statistical Science*, pages 457–472, 1992.
- Andrew Gelman et al. Prior distributions for variance parameters in hierarchical models (comment on article by Browne and Draper). *Bayesian Analysis*, 1(3):515–534, 2006.
- Douglas James Gerrard. *Competition quotient: A new measure of the competition affecting individual forest trees*, volume 20. Agricultural Experiment Station, Michigan State University, 1969.
- Robert J Gillies, Daniel Verduzco, and Robert A Gatenby. Evolutionary dynamics of carcinogenesis and why targeted therapy does not work. *Nature Reviews Cancer*, 12(7): 487–493, 2012.

- Donald F Gleason, George T Mellinger, Veretans Administration Cooperative Urological Research Group, et al. Prediction of prognosis for prostatic adenocarcinoma by combined histological grading and clinical staging. *The Journal of Urology*, 167(2):953–958, 2002.
- Pavel Grabarnik, Mari Myllymäki, and Dietrich Stoyan. Correct testing of mark independence for marked point patterns. *Ecological Modelling*, 222(23):3888–3894, 2011.
- John M Hammersley and Peter Clifford. Markov fields on finite graphs and lattices. 1971.
- Douglas Hanahan and Robert A Weinberg. Hallmarks of cancer: the next generation. *Cell*, 144(5):646–674, 2011.
- A Hughes. Cat retina and the sampling theorem: The relation of transient and sustained brisk-unit cut-off frequency to α and β -mode cell density. *Experimental Brain Research*, 42(2):196–202, 1981a.
- A Hughes. Population magnitudes and distribution of the major modal classes of cat retinal ganglion cell as estimated from hrp filling and a systematic survey of the soma diameter spectra for classical neurones. *Journal of Comparative Neurology*, 197(2):303–339, 1981b.
- Jung Wook Huh, Jae Hyuk Lee, and Hyeong Rok Kim. Prognostic significance of tumor-infiltrating lymphocytes for patients with colorectal cancer. *Archives of Surgery*, 147(4):366–372, 2012.
- Elliot E Hui and Sangeeta N Bhatia. Micromechanical control of cell–cell interactions. *Proceedings of the National Academy of Sciences*, 104(14):5722–5726, 2007.
- Janine Illian, Antti Penttinen, Helga Stoyan, and Dietrich Stoyan. *Statistical analysis and modelling of spatial point patterns*, volume 70. John Wiley & Sons, 2008.

- Melissa R Junttila and Frederic J de Sauvage. Influence of tumour micro-environment heterogeneity on therapeutic response. *Nature*, 501(7467):346–354, 2013.
- Yohei Kashima. Exponential decay of correlation functions in many-electron systems. *Journal of Mathematical Physics*, 51(6):063521, 2010.
- Qianyun Li, Faliu Yi, Tao Wang, Guanghua Xiao, and Faming Liang. Lung cancer pathological image analysis using a hidden Potts model. *Cancer Informatics*, page Accepted, 2017.
- Faming Liang. A double Metropolis–Hastings sampler for spatial models with intractable normalizing constants. *Journal of Statistical Computation and Simulation*, 80(9):1007–1022, 2010.
- Faming Liang, Ick Hoon Jin, Qifan Song, and Jun S Liu. An adaptive exchange algorithm for sampling from distributions with intractable normalizing constants. *Journal of the American Statistical Association*, 111(513):377–393, 2016.
- MNM van Lieshout and AJ Baddeley. A nonparametric measure of spatial interaction in point patterns. *Statistica Neerlandica*, 50(3):344–361, 1996.
- HW Lotwick and BW Silverman. Methods for analysing spatial processes of several types of points. *Journal of the Royal Statistical Society. Series B (Methodological)*, pages 406–413, 1982.
- Xin Luo, Xiao Zang, Lin Yang, Junzhou Huang, Faming Liang, Jaime Rodriguez Canales, Ignacio I Wistuba, Adi Gazdar, Yang Xie, and Guanghua Xiao. Comprehensive computational pathological image analysis predicts lung cancer prognosis. *Journal of Thoracic Oncology*, 2016.

- Alberto Mantovani, Silvano Sozzani, Massimo Locati, Paola Allavena, and Antonio Sica. Macrophage polarization: tumor-associated macrophages as a paradigm for polarized M2 mononuclear phagocytes. *Trends in Immunology*, 23(11):549–555, 2002.
- Torsten Mattfeldt, Stefanie Eckel, Frank Fleischer, and Volker Schmidt. Statistical analysis of labelling patterns of mammary carcinoma cell nuclei on histological sections. *Journal of Microscopy*, 235(1):106–118, 2009.
- Lauren MF Merlo, John W Pepper, Brian J Reid, and Carlo C Maley. Cancer as an evolutionary and ecological process. *Nature Reviews Cancer*, 6(12):924–935, 2006.
- Jesper Møller, Anthony N Pettitt, R Reeves, and Kasper K Berthelsen. An efficient markov chain monte carlo method for distributions with intractable normalising constants. *Biometrika*, 93(2):451–458, 2006.
- Iain Murray, Zoubin Ghahramani, and David MacKay. MCMC for doubly-intractable distributions. *arXiv preprint arXiv:1206.6848*, 2012.
- Akira Orimo, Piyush B Gupta, Dennis C Sgroi, Fernando Arenzana-Seisdedos, Thierry De-launay, Rizwan Naeem, Vincent J Carey, Andrea L Richardson, and Robert A Weinberg. Stromal fibroblasts present in invasive human breast carcinomas promote tumor growth and angiogenesis through elevated SDF-1/CXCL12 secretion. *Cell*, 121(3):335–348, 2005.
- L Peichl and H Wässle. Morphological identification of on-and off-centre brisk transient (y) cells in the cat retina. In *Proceedings of the Royal Society of London B: Biological Sciences*, volume 212, pages 139–153. The Royal Society, 1981.
- Oliver Penrose and Joel L Lebowitz. On the exponential decay of correlation functions. *Communications in Mathematical Physics*, 39(3):165–184, 1974.

- Kornelia Polyak, Izhak Haviv, and Ian G Campbell. Co-evolution of tumor cells and their microenvironment. *Trends in Genetics*, 25(1):30–38, 2009.
- Adrian E Raftery and Steven M Lewis. Practical Markov chain Monte Carlo: comment: one long run with diagnostics: implementation strategies for markov chain monte carlo. *Statistical Science*, 7(4):493–497, 1992.
- Julián Rincón, Martin Ganahl, and Guifre Vidal. Lieb-Liniger model with exponentially decaying interactions: A continuous matrix product state study. *Physical Review B*, 92(11):115107, 2015.
- B. D. Ripley and J. P. Rasson. Finding the edge of a poisson forest. *Journal of Applied Probability*, 14(3):483–491, 1977.
- Brian D Ripley. Modelling spatial patterns. *Journal of the Royal Statistical Society. Series B (Methodological)*, pages 172–212, 1977.
- Rebecca L Rockhill, Thomas Euler, and Richard H Masland. Spatial order within but not between types of retinal neurons. *Proceedings of the National Academy of Sciences*, 97(5):2303–2307, 2000.
- David M Segal and David A Stephany. The measurement of specific cell: Cell interactions by dual-parameter flow cytometry. *Cytometry Part A*, 5(2):169–181, 1984.
- Shinichiro Shirota and Alan E Gelfand. Inference for log gaussian cox processes using an approximate marginal posterior. *arXiv preprint arXiv:1611.10359*, 2016.
- Dietrich Stoyan and Antti Penttinen. Recent applications of point process methods in forestry statistics. *Statistical Science*, pages 61–78, 2000.

- Ming-Sound Tsao, Sophie Marguet, Gwénaél Le Teuff, Sylvie Lantuejoul, Frances A Shepherd, Lesley Seymour, Robert Kratzke, Stephen L Graziano, Helmut H Popper, Rafael Rosell, et al. Subtype classification of lung adenocarcinoma predicts benefit from adjuvant chemotherapy in patients undergoing complete resection. *Journal of Clinical Oncology*, 33(30):3439–3446, 2015.
- MNM Van Lieshout and Adrian J Baddeley. Indices of dependence between types in multivariate point patterns. *Scandinavian Journal of Statistics*, 26(4):511–532, 1999.
- David I Vaney, Leo Peichl, and BB Boycott. Matching populations of amacrine cells in the inner nuclear and ganglion cell layers of the rabbit retina. *Journal of Comparative Neurology*, 199(3):373–391, 1981.
- Luc Vincent and Dominique Jeulin. Minimal paths and crack propagation simulations. *Acta Stereologica*, 8(2):487–494, 1989.
- H Wässle and R-B Illing. Morphology and mosaic of on-and off-beta cells in the cat retina and some functional considerations. In *Proceedings of the Royal Society of London B: Biological Sciences*, volume 212, pages 177–195. The Royal Society, 1981.
- H Wässle and L Peichl. Morphology and topography of on-and off-alpha cells in the cat retina. In *Proceedings of the Royal Society of London B: Biological Sciences*, volume 212, pages 157–175. The Royal Society, 1981.
- H Wässle and HJ Riemann. The mosaic of nerve cells in the mammalian retina. In *Proceedings of the Royal Society of London B: Biological Sciences*, volume 200, pages 441–461. The Royal Society, 1978.

- H Wässle, L Peichl, and BB Boycott. Topography of horizontal cells in the retina of the domestic cat. In *Proceedings of the Royal Society of London B: Biological Sciences*, volume 203, pages 269–291. The Royal Society, 1978.
- H Wässle, L Peichl, and BB Boycott. Dendritic territories of cat retinal ganglion cells. *Nature*, 292(5821):344, 1981.
- Thorsten Wiegand and Kirk A Moloney. Rings, circles, and null-models for point pattern analysis in ecology. *Oikos*, 104(2):209–229, 2004.
- Bryony S Wiseman and Zena Werb. Stromal effects on mammary gland development and breast cancer. *Science*, 296(5570):1046–1049, 2002.
- Guanghua Xiao, Cavan Reilly, and Arkady B Khodursky. Improved detection of differentially expressed genes through incorporation of gene locations. *Biometrics*, 65(3):805–814, 2009.
- Guanghua Xiao, Xinlei Wang, and Arkady B Khodursky. Modeling three-dimensional chromosome structures using gene expression data. *Journal of the American Statistical Association*, 106(493):61–72, 2011.
- Kun-Hsing Yu, Ce Zhang, Gerald J Berry, Russ B Altman, Christopher Ré, Daniel L Rubin, and Michael Snyder. Predicting non-small cell lung cancer prognosis by fully automated microscopic pathology image features. *Nature Communications*, 7, 2016.
- Yinyin Yuan, Henrik Failmezger, Oscar M Rueda, H Raza Ali, Stefan Gräf, Suet-Feung Chin, Roland F Schwarz, Christina Curtis, Mark J Dunning, Helen Bardwell, et al. Quantitative image analysis of cellular heterogeneity in breast tumors complements genomic profiling. *Science Translational Medicine*, 4(157):157ra143, 2012.

Table 6: Lung cancer case study: The P -values of the transformed model parameters by fitting a Cox regression model with survival time and vital status as responses, and $\hat{\phi}_{\text{str,lym}}$, $\hat{\phi}_{\text{tum,lym}}$, $\hat{\phi}_{\text{lym,str}}$, $\hat{\phi}_{\text{tum,str}}$, $\hat{\phi}_{\text{lym,tum}}$, $\hat{\phi}_{\text{str,tum}}$, $\hat{\pi}_{\text{lym}}$, $\hat{\pi}_{\text{str}}$, $\hat{\lambda}$, age, gender, and smoking history as predictors. The overall P -value corresponding to a Wald test for the model is 0.0024.

Predictor	Coefficient	exp(Coef.)	SE	P -value
$\hat{\phi}_{\text{str,lym}}$	13.22	5.5×10^5	5.16	0.15
$\hat{\phi}_{\text{tum,lym}}$	2.34	10.39	2.45	0.62
$\hat{\phi}_{\text{lym,str}}$	-0.59	0.55	0.76	0.68
$\hat{\phi}_{\text{tum,str}}$	8.83	6.8×10^3	1.60	0.0073
$\hat{\phi}_{\text{lym,tum}}$	-0.53	0.59	0.81	0.70
$\hat{\phi}_{\text{str,tum}}$	-6.08	2.3×10^{-3}	1.88	0.12
$\hat{\pi}_{\text{lym}}$	3.44	31.2	1.49	0.17
$\hat{\pi}_{\text{str}}$	-3.21	4.0×10^{-2}	0.72	0.017
$\hat{\lambda}$	-0.01	0.99	2.6×10^{-3}	0.19
Age	0.04	1.04	8.7×10^{-3}	0.17
Female vs. male	-0.12	0.89	9.1×10^{-2}	0.67
Smoking vs. non-smoking	0.07	1.07	8.9×10^{-2}	0.80

Table 7: Lung cancer case study: The P -values of $\text{MCF}_{\text{lym, str}}(0.1)$, $\text{MCF}_{\text{lym, tum}}(0.1)$, and $\text{MCF}_{\text{str, tum}}(0.1)$ by fitting a Cox regression model with survival time and vital status as responses, and $\text{MCF}_{\text{lym, str}}(0.1)$, $\text{MCF}_{\text{lym, tum}}(0.1)$, $\text{MCF}_{\text{str, tum}}(0.1)$, proportion of lymphocyte cells, proportion of stromal cells, age, gender, and smoking history as predictors. The overall P -value corresponding to a Wald test for the model is 0.47.

Predictor	Coefficient	exp(Coef.)	SE	P -value
$\text{MCF}_{\text{lym, str}}(d = 0.1)$	-2.92	0.05	1.38	0.23
$\text{MCF}_{\text{lym, tum}}(d = 0.1)$	-0.63	0.53	0.47	0.54
$\text{MCF}_{\text{str, tum}}(d = 0.1)$	0.12	1.12	0.79	0.95
Prop. of lym cells	0.75	2.11	0.25	0.16
Prop. of str cells	-0.31	0.73	0.61	0.79
Age	0.03	1.03	0.01	0.21
Female vs. male	-0.17	0.84	0.09	0.56
Smoking vs. non-smoking	0.07	1.07	0.09	0.81